Mean Circulation and Internal Variability in an Ocean Primitive Equation Model

Sybren Drijfhout, Christoph Heinze, Mojib Latif, and Ernst Maier-Reimer

Max-Planck-Institut für Meteorologie, Hamburg, Germany

(Manuscript received 28 November 1994, in final form 20 September 1995)

ABSTRACT

A primitive equation World Ocean model has been integrated with restoring boundary conditions to reach a steady state. The global distribution of potential temperature, salinity, and meridional streamfunction are consistent with observations. In steady state, the effective freshwater fluxes were diagnosed, and the model has been integrated further prescribing these freshwater fluxes.

The ocean circulation undergoes self-sustained oscillations over a wide range of timescales, ranging from decadal to millennium. Most pronounced are self-sustained oscillations with a timescale of 20, 300, and 1000 years. The latter two oscillations are coupled. They consist of density (salinity) anomalies that circulate through the global conveyor belt, periodically enhancing convection in the Southern Ocean and limiting convection in the northern North Atlantic. The timescale is set by the vertical diffusion, which destabilizes the stratification in the Southern Ocean when convection is weak. The 20-yr oscillation is a coupled salinity and sea ice thickness anomaly propagating around Antarctica.

1. Introduction

Through the redistribution of heat and freshwater (or salt) the oceanic general circulation is a major factor in controlling the present climate. Also, the ocean is believed to play a key role in forcing climate variations, especially on timescales ranging from interannual to millennium. The oceans react in a nonlinear way to changes in the atmospheric forcing. One reason for this strong sensitivity results from the fact that the ocean is marginally hydrostatically stable in several regions. Small perturbations in the atmospheric forcing can drastically change patterns of convection in the ocean. Subsequently, the meridional heat transport is changed, which in turn influences the atmosphere. By this process, the oceans response to changes in the atmospheric forcing provides feedbacks in the coupled ocean–atmosphere system. Broecker et al. (1988), for example, conjecture that such an ocean–atmosphere feedback might be responsible for the Younger Dryas event. In a recent paper, Maier-Reimer et al. (1993, hereafter abbreviated MMH) have established the sensitivity of the oceanic general circulation to thermohaline forcing. They found completely different circulation regimes under slightly different atmospheric forcing, while all forcings were acceptable interpretations of the present climatology within its bounds of uncertainty.

The oceans can also introduce variability in the climate system by integrating the high-frequency weather fluctuations into an essentially red spectrum. This occurs when the long timescales of the oceanic circulation are separated from the short timescales of the atmospheric forcing (Hasselmann 1976). A negative (linear) feedback is required to limit the variability at low frequencies. This process has been confirmed by observations (Frankignoul and Hasselmann 1977) and by modeling studies (Mikolajewicz and Maier-Reimer (1990, hereafter abbreviated MMR). The latter have run an ocean general circulation model under mixed boundary conditions (a flux condition on surface salinity and a restoring condition on surface temperature) with temporally white but spatially coherent freshwater flux perturbations added. The spectrum of oceanic variability roughly matched a red noise spectrum, assuming a linear negative feedback with a timescale of 500 years. The energy on timescales from 50 to 500 years, however, was considerably higher than predicted by Hasselmann's stochastic climate model theory, due to the internal dynamics of the ocean, which may organize variability in specific eigenmodes. An eigenmode with a 320-yr period was most pronounced in their study.

Another form of oceanic variability results from the existence of multiple equilibria of the ocean's thermohaline circulation (THC) when mixed boundary conditions are applied. The existence of multiple equilibria was suggested by Stommel (1961) and Rooth (1982), and the theory was supported by numerical experiments by, for example, Bryan (1986) and Marotzke et al. (1988) using idealized ocean models and by Manabe and Stouffer (1988) with a coupled

Corresponding author address: Dr. Sybren Drijfhout, Royal Netherlands Meteorological Institute, P.O. Box 201, 3730 AE De Bilt, the Netherlands.
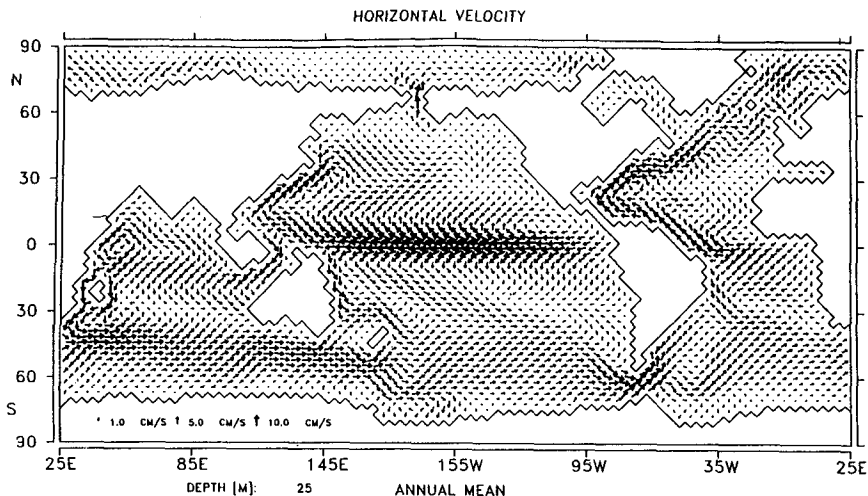E-mail: dryfhout@knmi.nl

FIG. 1. Horizontal velocity at 25 m (surface layer).

ocean–atmosphere model. The ocean circulation can switch from one to another equilibrium, and the transition can occur on a decadal timescale (polar halocline catastrophe).

Self-sustained oscillations can also occur, applying constant atmospheric forcing (e.g., Marotzke 1990; Weaver and Sarachik 1991; Winton and Sarachik 1993). They can be explained by a Hopf bifurcation, which is introduced by the change of a parameter. The Hopf bifurcation is associated with a dynamical regime where certain classes of perturbations can extract energy from the mean state. Up to now, self-sustained oscillations have been found mostly in idealized models. Moore and Reason (1993) used the Princeton World Ocean model to study the response to mixed boundary conditions and did not find self-sustained oscillations, unless a flat bottom version was used. The

control run without noise of MMR was also steady. However, Pierce et al. (1995) have been able to recover the eigenmode found in the noise run of MMR without any noise added to the forcing fields, but with an altered forcing field with respect to MMR. This suggests that the parameter range under which self-sustained oscillations occur might be small. Delworth et al. (1993) found an interdecadal oscillation in a realistic coupled ocean–atmosphere model. However, it cannot be concluded whether this oscillation of the ocean circulation is self-sustained or an oceanic eigenmode excited by atmospheric forcing.

So far, it is not clear to what extent model results on oceanic internal variability are model dependent and to what extent they carry over into the real world. As the number of realistic World Ocean models used for climate variability studies is rather small [mainly the
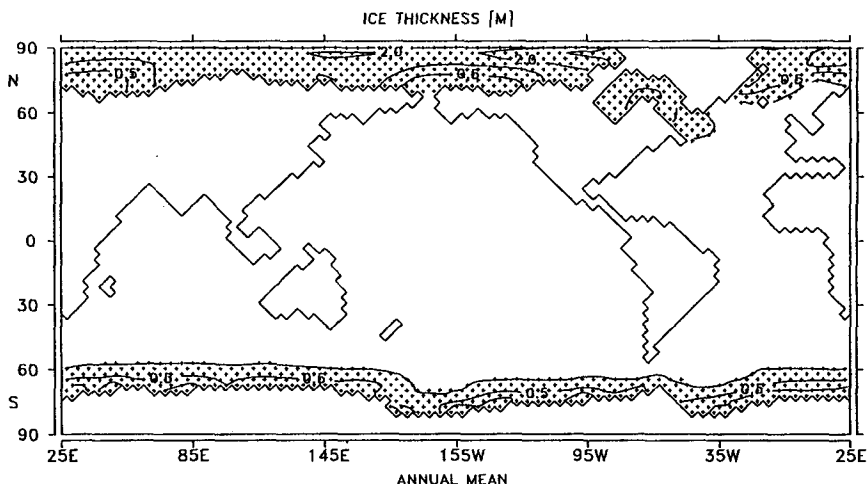

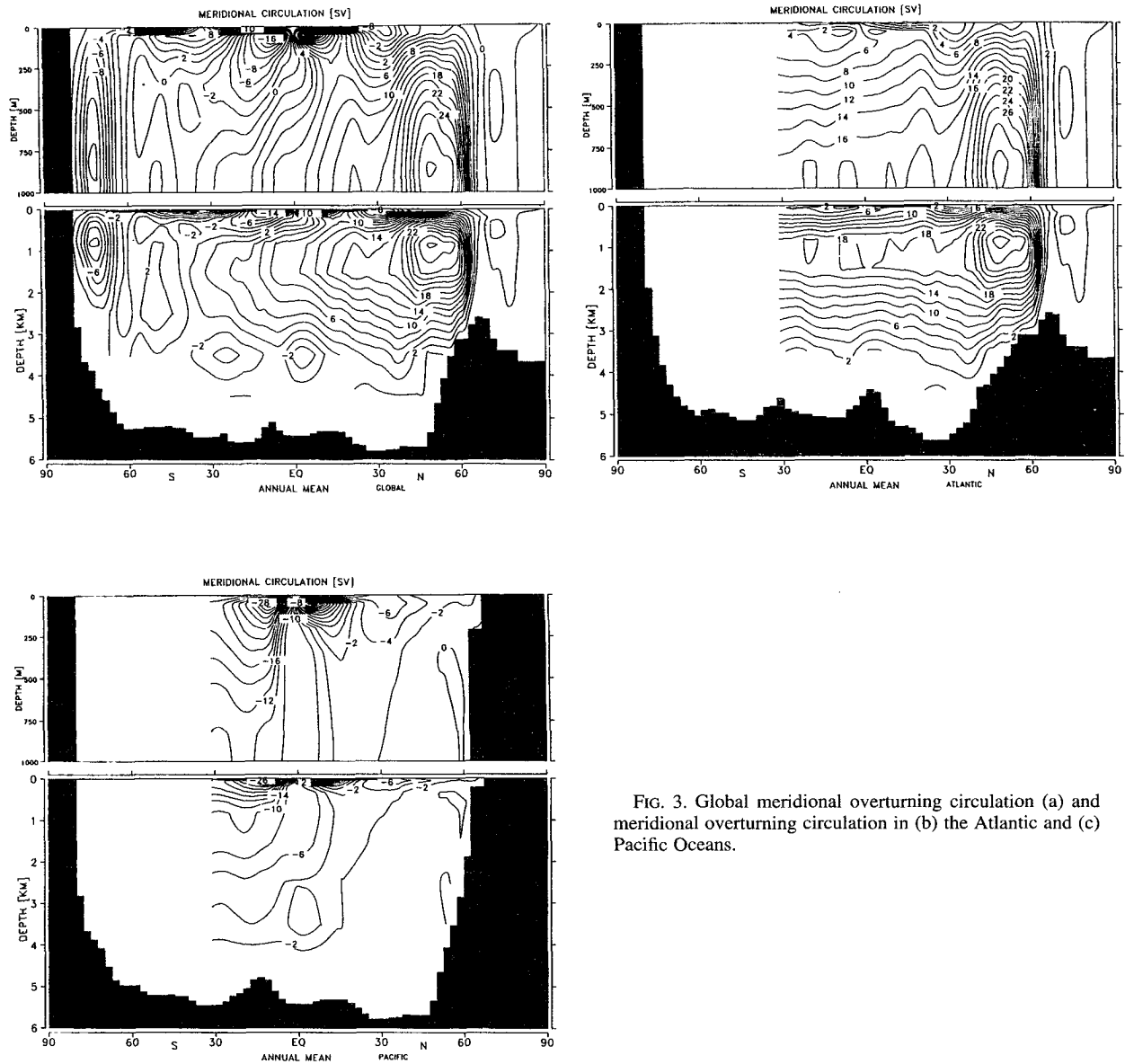
FIG. 2. Yearly averaged sea ice thickness (in m).

FIG. 3. Global meridional overturning circulation (a) and meridional overturning circulation in (b) the Atlantic and (c) Pacific Oceans.

Hamburg Large Scale Geostrophic (LSG) Model and the Princeton Geophysical Fluid Dynamics Laboratory (GFDL) Model], the results published so far may be biased toward specific model characteristics. Here, we present a World Ocean model based on the primitive equation and examine its response to climatological forcing. It will be shown that the model displays self-sustained oscillations when using mixed boundary conditions.

The main differences relative to the well-known standard GFDL primitive equation model (e.g., Cox 1984) are the dynamically active free surface [an alternative version of the GFDL model with a free surface was developed by Killworth et al. (1991)], the (partial) use of implicit methods to solve the momen-

tum equations, the more detailed representation of the bottom topography, and the use of a dynamic thermodynamic sea ice model with a viscous–plastic constitutive law to describe the variation of rheology based on Hibler (1979). The main differences relative to the Hamburg Large Scale Geostrophic Model (e.g., MMH) are the inclusion of the nonlinear momentum advection, the explicit formulation of horizontal and vertical diffusivities, a considerably shorter time step, the more sophisticated sea ice model, and the use of a centered difference scheme instead of an upstream method for tracer advection.

The paper is organized as follows. In section 2, a general description of the model is given. The mean ocean circulation is described in section 3. In sections
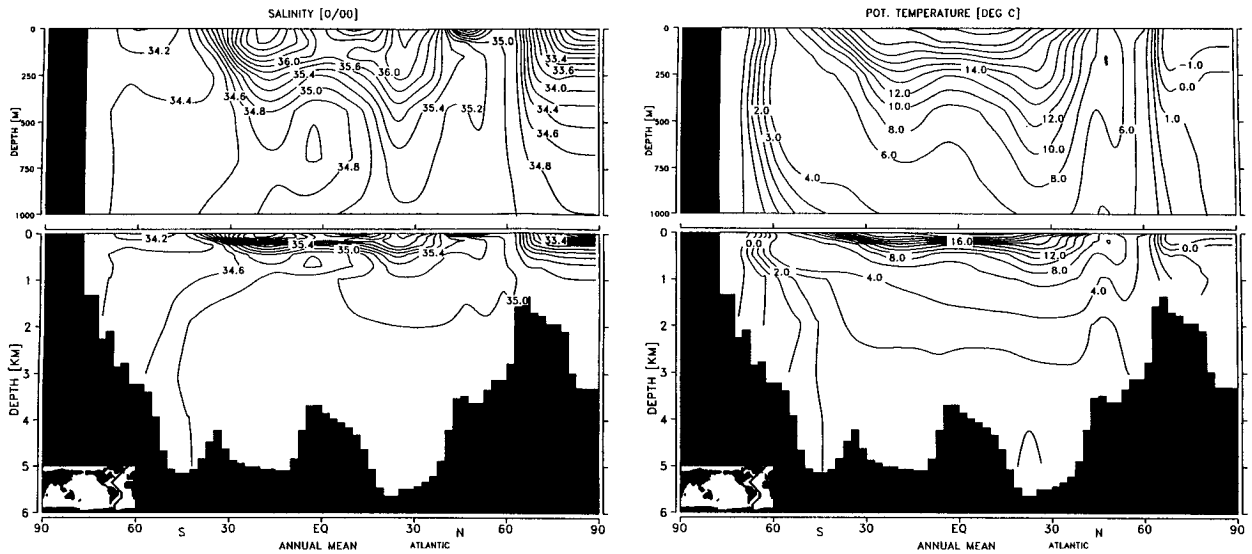
FIG. 4. Simulated (a) salinity and (b) potential temperature along the GEOSECS section in the Atlantic.

4 and 5, the run with mixed boundary conditions is discussed. The paper is concluded in section 6.

2. Model description

The ocean general circulation model is an extended version of the model described by, for example, Latif (1987) and Latif et al. (1994). It is based on the nonlinear balance equations for momentum (the equations of motion), the continuity equation for an incompressible fluid, and conservation equations for temperature and salinity. The model employs the hydrostatic and Boussinesq approximations. The prognostic variables are horizontal velocities, sea surface elevation, temperature and salinity, and sea ice thickness and compactness.

The horizontal momentum balance equations are (here written schematically in rectilinear coordinates for simplicity)

$$\frac{d\mathbf{u}}{dt} + f(\mathbf{k} \times \mathbf{u})$$

$$= -\frac{1}{\rho_0}[\nabla_H(p + \rho_0 g\zeta)] + F_H + F_V, \quad (2.1)$$

where $\mathbf{u} = (u, v)$ is the horizontal velocity vector, f the Coriolis parameter, $\mathbf{k}$ the vertical unit vector, ρ_0 a reference density, g the gravitational acceleration, $p = g \int_h^0 \rho dz$ the internal pressure and ζ the sea surface elevation.

The horizontal and vertical turbulent viscous terms F_H and F_V are formulated according to K theory. Harmonic, biharmonic, and local strain-dependent friction are successively applied. In general, the harmonic friction dominates the other terms, which are mainly op-

erative to suppress the grid-scale noise. The harmonic viscosity parameter A_H is grid-size dependent. It is 3 $\times$ 10^5 m^2 s^{-1} at the equator, otherwise proportional to the relative surface of the grid box. The vertical eddy viscosity parameter A_V is 2.0×10^{-4} m^2 s^{-1}.

The internal pressure is computed from the density field using the hydrostatic approximation. The density is calculated using the UNESCO (1983) formula. The vertical velocity w is calculated diagnostically from the continuity equation. In case of unstable stratification, convective adjustment is applied; that is, each pair of vertically adjacent grid cells is perfectly mixed under consideration of heat and salt conservation.

The sea level elevation is calculated from the linearized kinematic boundary condition

$$\frac{\partial \zeta}{\partial t} = w|_{z=0} = -\nabla_H \int_{-H}^0 \mathbf{u} dz, \quad (2.2)$$

$H(\phi, \lambda)$ being the water depth. The model is forced at the sea surface by climatological surface wind stress data, based on monthly mean values taken from Hellerman and Rosenstein (1983). Bottom friction is computed applying a Newtonian friction law. No-slip boundary conditions are used at lateral boundaries.

To solve the momentum equations (2.1), a method of fractional steps is used. First, (2.1) is solved omitting the nonlinear advection terms and the viscous dissipation. The velocities are decomposed into a barotropic and baroclinic part. Then, the barotropic velocities are solved implicitly by direct matrix inversion. The baroclinic subsystem is written in a semi-implicit form and solved by an iterative method. Nonlinear advection is computed with a discretization scheme that guarantees both conservation of kinetic energy and enstrophy (Arakawa and Lamb 1977). Vertical advection

HEAT FLUX (DIAGNOSTIC) [W/M**2]
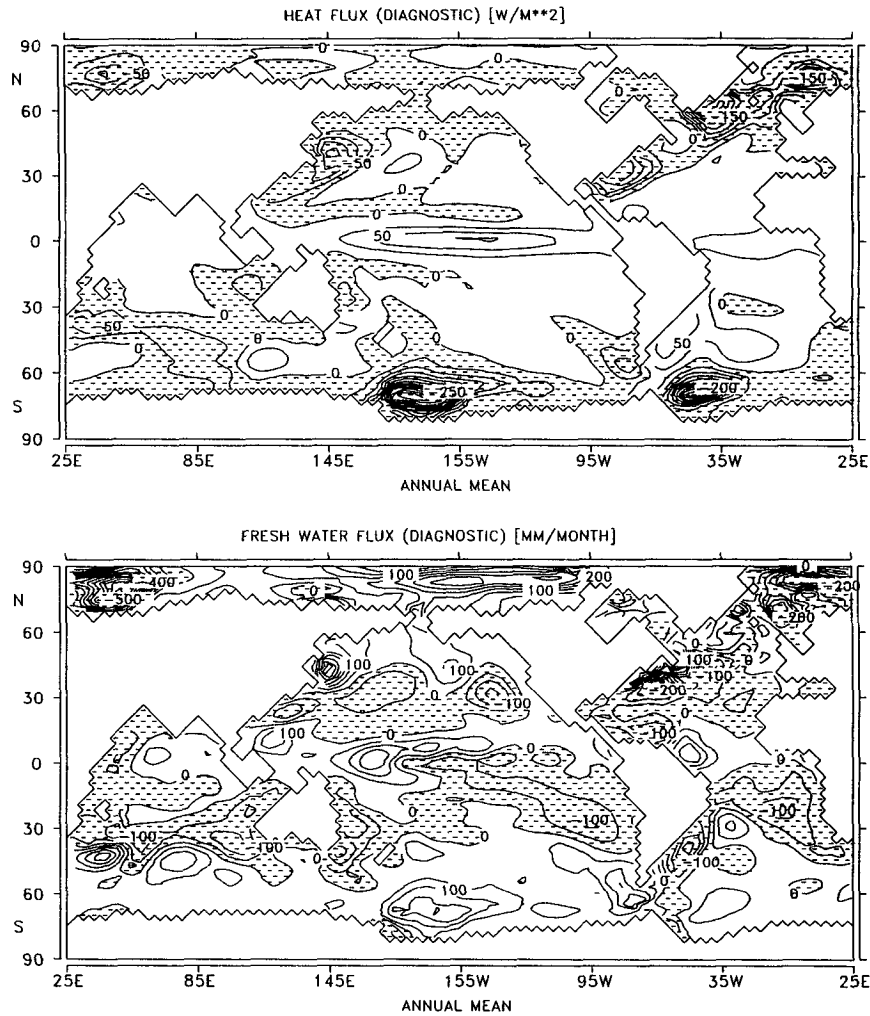

FRESH WATER FLUX (DIAGNOSTIC) [MM/MONTH]

FIG. 5. (a) Heat flux as determined diagnostically from the temperature boundary condition and (b) freshwater flux diagnosed from the salinity boundary condition. Positive fluxes are going into the ocean.

and mixing are computed implicitly. Horizontal mixing is computed by an explicit method.

Potential temperature θ and salinity S are prognostic variables determined by the transport equations

$$\frac{d\theta}{dt} = D_V \frac{\partial^2 \theta}{\partial z^2} + D_H \nabla_H^2 \theta \qquad (2.3)$$

$$\frac{dS}{dt} = D_V \frac{\partial^2 S}{\partial z^2} + D_H \nabla_H^2 S \qquad (2.4)$$

with horizontal and vertical eddy diffusivity coefficients D_H and D_V. The horizontal diffusivity parameter D_H is 2000 m^2 s^{-1}; the vertical mixing parameter D_V is 0.5×10^{-4} m^2 s^{-1}. The surface fields are relaxed to climatological fields (θ^*, S^*). Temperature is restored to monthly mean air temperature from the COADS dataset (Woodruff et al. 1987) with a timescale of 80

days. Salinity is restored to the annual mean sea surface salinity (Levitus 1982) with a timescale of 40 days. Compared to MMH the restoring time for temperature is increased by 20 days (it is generally believed that the effective restoring time for large-scale temperature anomalies should be more than 100 days; e.g., Mikolajewicz and Maier-Reimer 1994). Solar radiation is parameterized by a simple geometrical function, dependent on the latitude and the day of the year. Maximum input is 63 W m^{-2} in the surface layer of 50 m (this value was tuned to maintain the globally averaged SST).

The salinity boundary condition forces also changes in ζ by calculating the equivalent freshwater flux. At lateral boundaries and the seafloor no-flux conditions apply for heat and salt. As in MMH, the effect of short-timescale synoptic processes in the atmosphere is parameterized by advection of air from the upstream di-
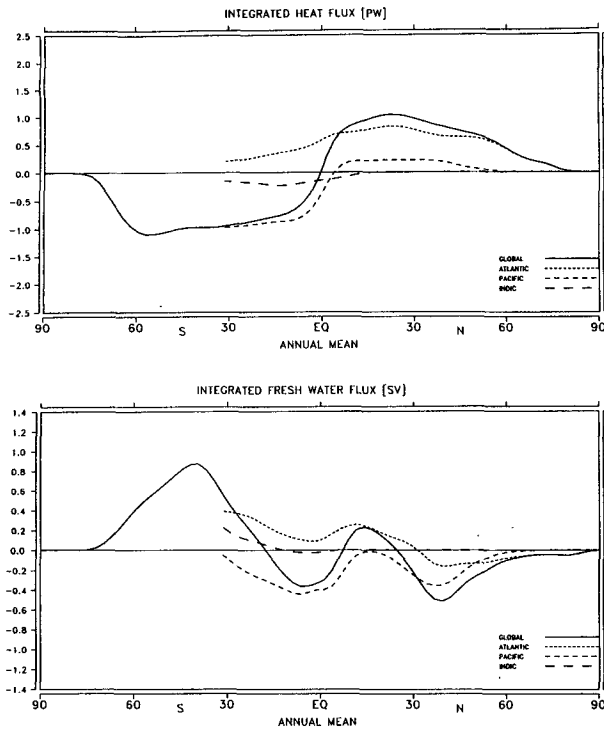
FIG. 6. (a) Zonally integrated transport of heat and (b) integrated freshwater flux out of the ocean.

occurs. The thermodynamical part of the sea ice model is coupled to the dynamical part by calculating the advective sea ice fluxes.

The model was run on a 5° × 5° global E-grid (Arakawa and Lamb 1977), yielding an effective grid-point spacing of 3.5°. In the vertical, 11 levels were used. Horizontal velocity, temperature, and salinity are defined at depth levels 25, 75, 150, 250, 450, 700, 1000, 2000, 3000, 4000, and 5000 m, and vertical velocity and pressure at intermediate levels. The model includes a realistic smoothed bottom topography. This model configuration is the same as the one used by MMH. Differences to MMH are a slightly longer advection timescale in the parameterization of subgrid-scale at-
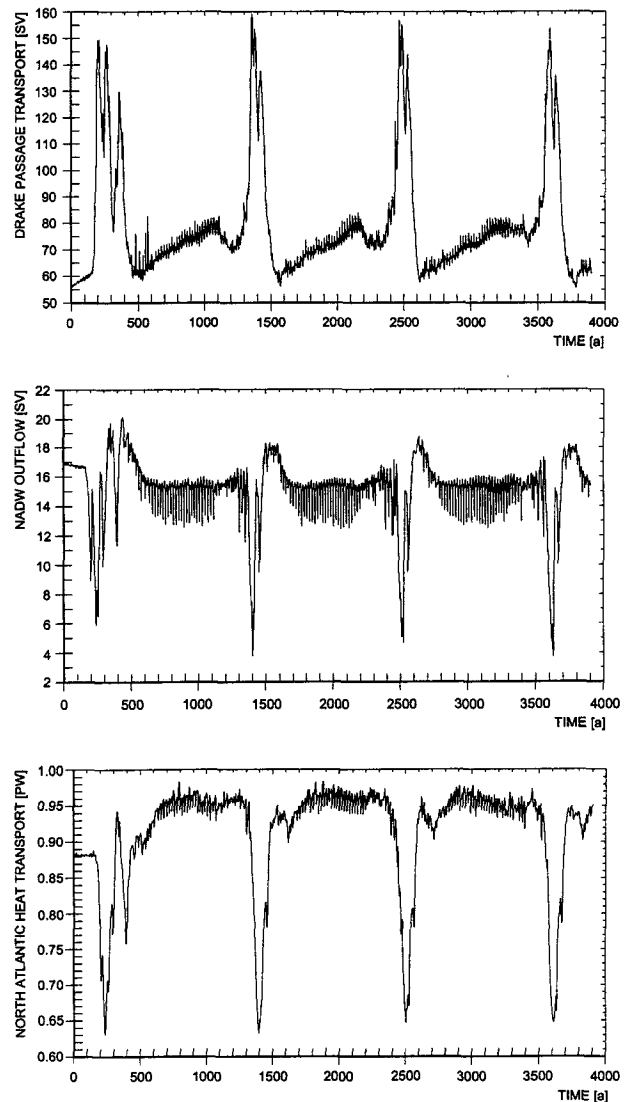
rection. The advective timescale is chosen to be 1.5 × 10⁵ s; see MMH for a discussion of this parameterization. The advection and horizontal diffusion of temperature and salinity are computed by a half-split method (Arakawa and Lamb 1977) (the same method used to compute the nonlinear horizontal momentum advection). Vertical mixing of the thermohaline fields is solved implicitly.

When seawater is cooled down to a temperature of −1.9°C, any additional cooling results in the formation of sea ice. The thermodynamic part of the ice model is formulated according to Stefan (1891). The variation of rheology is described with a viscous–plastic constitutive law according to Hibler (1979). The salinity is changed according to the volume change of the water column with total salt being conserved.

The air–sea heat flux is modified in the presence of sea ice by multiplication with a factor $(1 - A)$, the fraction of open water [A is the sea ice compactness (see Hibler 1979)]. We have chosen to leave the salinity boundary condition unaffected. The restoring condition on surface salinity is an artificial and unphysical method to keep the sea surface salinity close to observations, whether or not one accounts for the presence of sea ice; see Moore and Reason (1993) for more discussion on this issue.

When the sea surface temperature is higher than the freezing temperature while sea ice is present, melting

FIG. 7. Time series for (a) mass transport through Drake Passage, (b) mass volume of NADW outflow at 30°S, and (c) Atlantic heat transport at 30°N in petawatts.
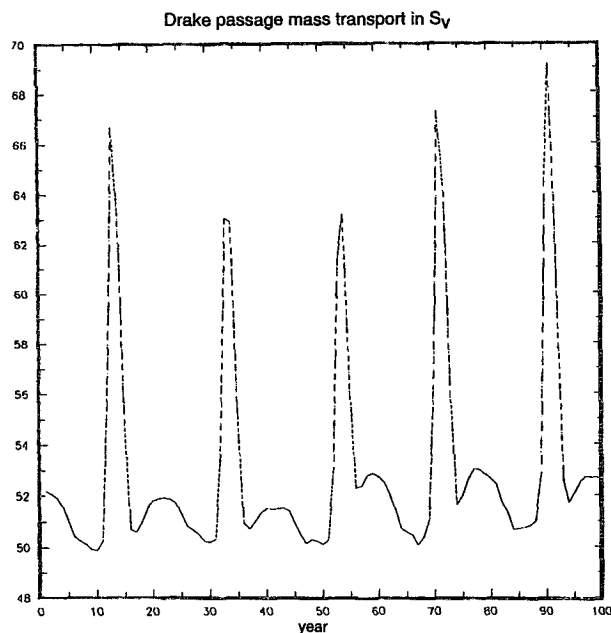
Drake passage mass transport in S_v

FIG. 8. Hundred-year time series for the mass transport through Drake Passage showing the 20-yr oscillation.

mospheric processes, an increase of the SST-restoring time from 60 to 80 days, and a different restoring condition for salinity in the presence of sea ice. In the present formulation the model runs with a time step of 20 h. For more details we refer to the technical report on the HOPE model, which describes the next (improved) cycle of the model.

3. Steady-state circulation

First, the model was spun up more than 10 000 years with restoring boundary conditions until an equilibrium was reached (the maximal remaining trends were 5 $\times$ 10^{-4} K and 1 $\times$ 10^{-4} psu per century). The basic structure of the annual mean circulation in the surface layer is shown in Fig. 1. The horizontal velocities consist of a superposition of the Ekman drift and the geostrophic current. The main surface current systems are reproduced except for the Brazil Current and North Equatorial Countercurrent, which is present in the eastern Pacific only (it appears more complete in the second and third layer). The averaged sea ice thickness is shown in Fig. 2.

The zonally averaged mean meridional circulation for the global, Atlantic, and Pacific Oceans are presented in Figs. 3a–c. Deep-water formation is found in the northern North Atlantic and the Southern Ocean. The differences in global meridional overturning relative to the LSG model are strongest in the Southern Ocean. The depth penetration of the Ekman cell at 60°S is considerably reduced. Also the overturning cell in the Southern Ocean, associated with Antarctic Bottom

Water (AABW) formation is two times weaker. The rate of North Atlantic Deep Water (NADW) outflow from the Atlantic into the World Ocean is about 17 Sv (Sv $\equiv$ 10^6 m^3 s^{-1}).

By the use of a second-order scheme for tracer advection, the effective mixing is reduced relative to the LSG model. This is illustrated by reduced upwelling through the thermocline in the Pacific (Fig. 3c, respectively 3c in MMH). Toggweiler and Samuels (1993) argue that there should be no (or a very weak) upwelling through the thermocline in the Pacific. As a consequence, the deep Pacific is too young in the LSG model, having a too large ventilation rate. This feature
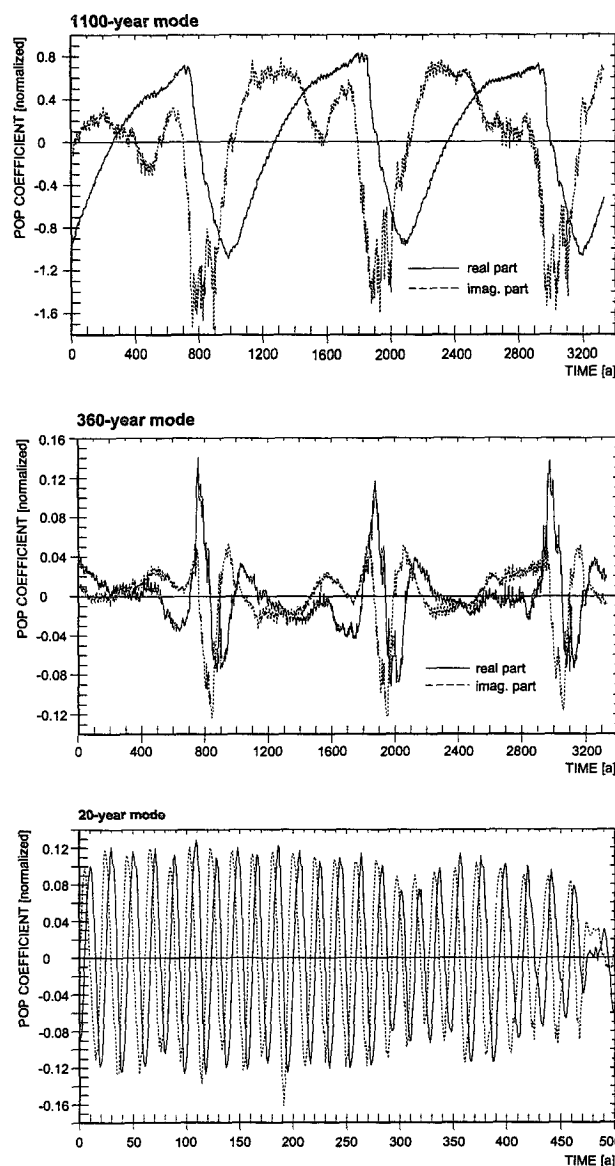

FIG. 9. Time series for POP coefficients of (a) 1100-yr mode, (b) 360-yr mode, (c) 20-yr mode. The real time series has a straight line; the imaginary is dashed.
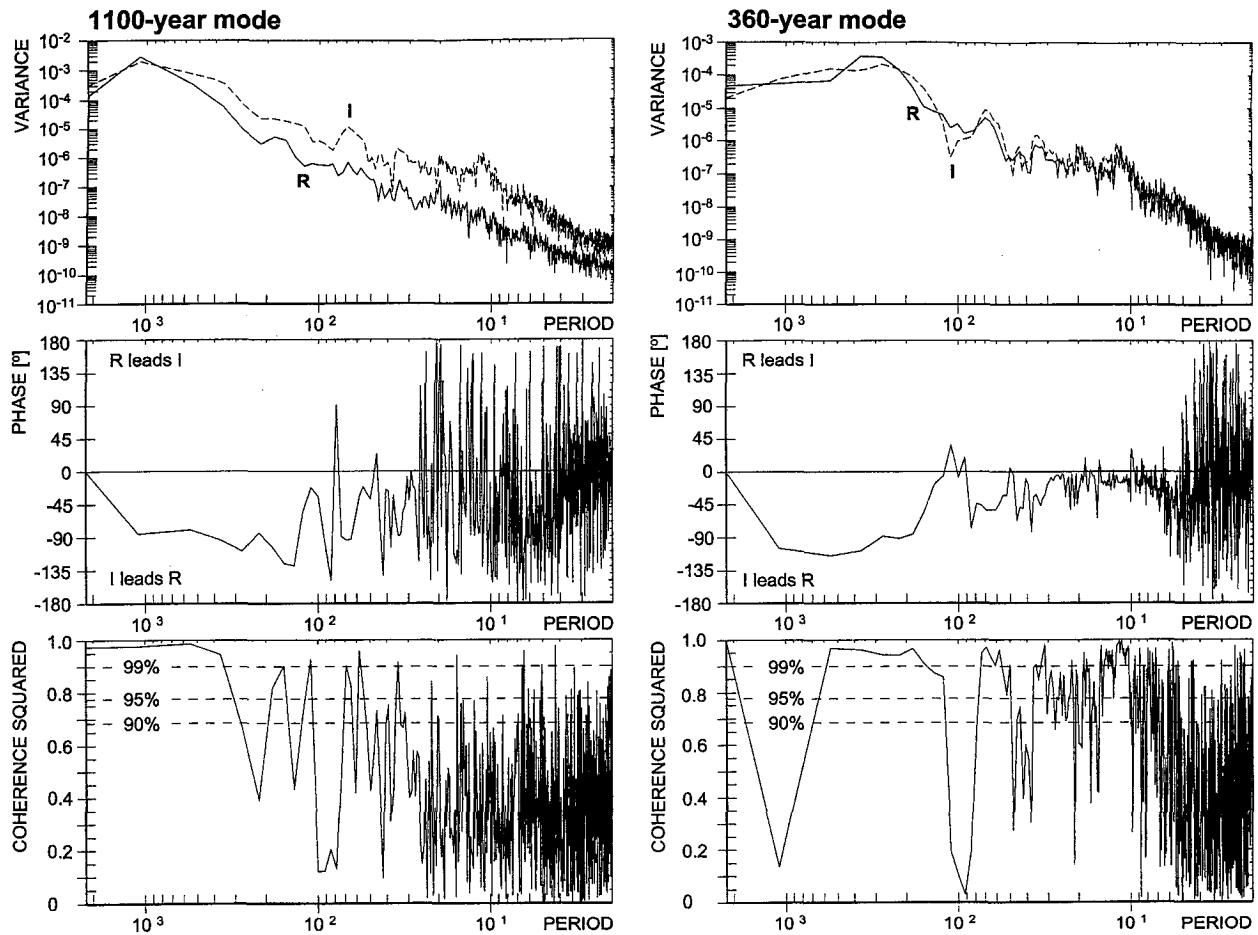
FIG. 10. Autospectra for time series of Fig. 9. The real part is denoted by **R**; the imaginary part by **I**.

is improved in the present model due to the reduced mixing. However, without additional passive tracer calculations it is difficult to conclude whether the overall circulation in the meridional plane has improved or not.

Compared to observations, the modeled characteristics of AABW are too cold and too fresh. This feature is consistent with findings using the GFDL model, which also uses a second-order scheme for tracer advection. England (1993) shows that the GFDL model produces too cold and too fresh AABW when restoring surface values to the Levitus data. The reason is that salinity near Antarctica has a pronounced seasonal cycle due to brine ejection when the seawater freezes. As winter measurements of salinity near Antarctica are rather scarce, the Levitus set is biased to too low values. England compensated for this effect by enhancing the surface salinity in the southernmost row in the model to values of 34.9 psu during the winter months. The GFDL model yields AABW with reasonable water mass characteristics only with this type of forcing. The stronger AABW formation in the LSG model, however, may be explained by the stronger effective mixing. The

relatively fresh waters south of the ACC are more often mixed with saltier waters from the north and below, which results in enhanced bottom water formation at higher temperature and salinity levels. We hypothesize that using a surface salinity boundary condition with enhanced winter values near Antarctica would intensify AABW formation in the present model and improve the deep ocean water mass characteristics. Also increasing the feedback parameter λ_2 will probably enhance the amount of AABW formation.

To elucidate the effect of the tracer advection scheme on the equilibrium solution, the model was run after reaching equilibrium with the second-order scheme, for another 1500 years using the upstream scheme. Although the model has not reached a complete steady state after 1500 years, the integration time is long enough to investigate the effect of the enhanced diffusivity. The global meridional streamfunction (not shown) shows a tremendous increase in AABW formation. This confirms the findings of Gerdes et al. (1991) that for low-resolution OGCMs the sensitivity of the results on the tracer advection scheme is strong.
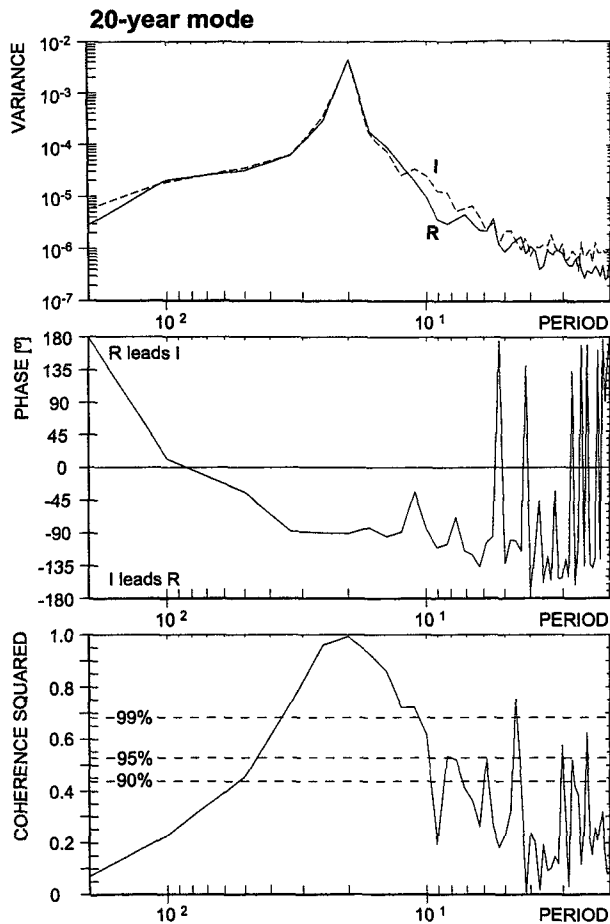
20-year mode

FIG. 10. (*Continued*)

The amount of AABW formation has a strong influence on the strength of the ACC. An enhancement of deep-water formation induces a larger density and pressure gradient across the ACC that, by geostrophy, induces larger zonal velocities. Also, locally increased zonal pressure gradients (i.e., across Drake Passage) accelerate the zonal momentum when ageostrophy is important. Using an upstream scheme, AABW formation is enhanced and the ACC is almost three times stronger. The too weak ACC (55 Sv) in the model with the second-order scheme is an indication that AABW formation is too weak. Below 700 m only a marginally small meridional density gradient exists across the ACC, and the current is almost absent there. Above 700 m where the current is dominantly wind-driven, the ACC is as strong as in the LSG model where the total transport is 120 Sv. Apparently, in low-resolution OGCMs one needs at least one of the following three remedies to get the strength of the ACC correct: 1) increasing the restoring values of the sea surface salinity near Antarctica in wintertime, 2) a widening and deepening of the Drake Passage, and 3) an enhance-

ment of the diffusivity. It should also be noted that the shorter restoring time for salinity compared to temperature used in the present model might suppress the AABW formation.

Figure 4 shows the distribution of S and T along the GEOSECS section in the Atlantic (cf. with Figs. 7 in MMH). The characteristics of NADW are rather close to observations. AABW, however, is somewhat too cool and too fresh. It should be noted that errors in temperature and salinity associated with AABW nearly compensate each other with respect to density. The low salinity tongue of the Antarctic Intermediate Water is clearly seen, although the feature is still somewhat too weak. In the Pacific, the simulated vertical temperature and salinity structures correspond well to the observations (not shown). The temperature stratification in the deep ocean, however, is somewhat too strong, and the salinity stratification too weak. The model does not show Antarctic Intermediate Water in the Pacific.

The surface fluxes of heat and freshwater diagnosed at steady state are shown in Fig. 5. Most remarkable is the strong heat loss in a relatively small area in the Ross Sea. Largest differences between the present and LSG model, however, appear in the Arctic region. Here, the influence of the different boundary condition under the sea ice is apparent. At present, low-resolution models are not capable of reproducing the complex salinity structure in the Arctic and sub-Arctic, which includes strong gradients and frontal features. As a result, large freshwater fluxes are needed to maintain this structure (Moore and Reason 1993).

Figure 6 shows the zonally integrated meridional transports of heat and freshwater. The absolute values are at the lower bounds of observations (Roemmich and Wunsch 1985). The relative shallow thermocline is likely to be responsible for this feature. Increasing the vertical diffusivity would enhance the heat transports. However, the deep-sea water mass characteristics would deteriorate. The heat transport in the Southern Ocean is relatively weak, consistent with a small AABW formation. The net freshwater transport between 80°N and 90°N is due to the relaxation of salinity under sea ice toward the Levitus values.

4. Internal variability: A statistical description

In steady state, the freshwater flux is diagnosed to maintain the sea surface salinities. As the model uses the sea surface height as a prognostic variable, the use of a freshwater flux boundary condition is straightforward. The pattern of the freshwater flux has a strong impact on the internal variability under mixed boundary conditions (Weaver et al. 1993). When switching from restoring to mixed boundary conditions our model yields self-sustained oscillations. The most important variability modes are strongest in the Southern Ocean. We expect, therefore, that their main characteristics are not strongly affected by the spurious freshwater fluxes in the Arctic Ocean.
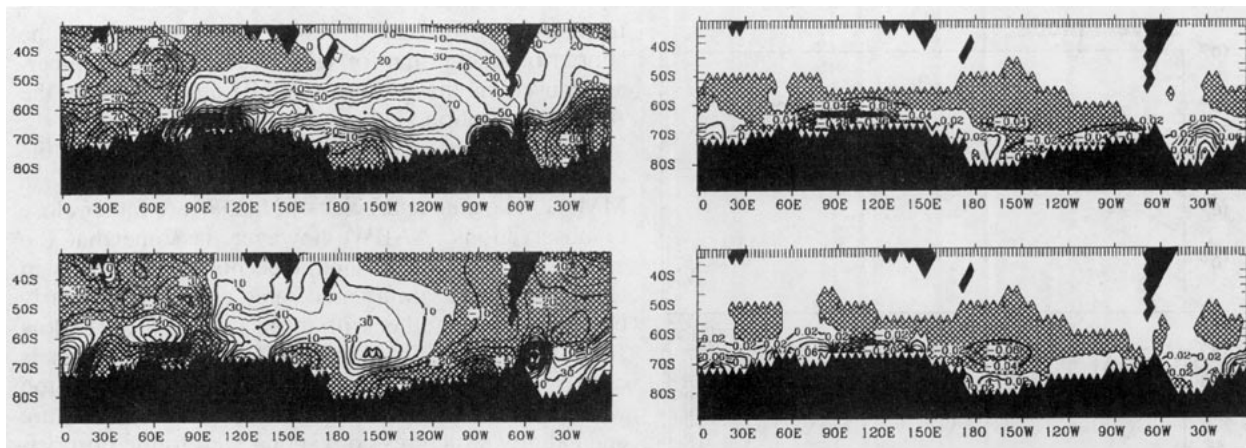
FIG. 11. POP pattern of (a) surface potential density (in 10^{-6} kg m^3) and (b) sea ice thickness (in m) for the 20-yr mode (above: the real part, below: the imaginary part).

Figure 7 shows three index time series: the time series of Drake Passage transport, outflow of NADW at 30°S, and Atlantic heat transport at 30°N. Most prominent are the large excursions in Drake Passage transport on a timescale of about 1100 years (Fig. 7a) that are associated with dips in NADW outflow and Atlantic heat transport (Figs. 7b and 7c). Outstanding in the three time series are also the higher-frequency variations. A more detailed analysis of the time series revealed that these oscillations have a period of about 20 years (Fig. 8). Considerable variability is also found on timescales of a few centuries.

In order to gain more insight into the space–time structure of the different variability modes, we performed two principal oscillation pattern (POP) analyses (Hasselmann 1988; Storch et al. 1995). POPs are designed to extract the dominant modes of variability from a multidimensional dataset. The POPs are the eigenvectors of the system matrix obtained by fitting the data to a multivariate first-order Markov process. The POPs are generally complex with real part p_1 and imaginary part p_2. These represent the spatial structure of the system. The corresponding complex coefficient time series A_i, which contain the information about the time evolution of the system, satisfy the standard damped harmonic oscillator equation, so that the evolution of the system in the two-dimensional POP space can be interpreted as a cyclic sequence of spatial patterns:

$$\cdots \rightarrow p_1 \rightarrow -p_2 \rightarrow -p_1 \rightarrow p_2 \rightarrow p_1 \rightarrow \cdots.$$

The characteristic period to complete a full cycle will be referred to as "rotation period" and the e-folding time for exponential decay as "damping time." Both timescales are estimated as part of the POP analysis.

Two POP analyses were performed. We used the global three-dimensional density field in the first POP analysis. Prior to the analysis, the data were smoothed

in time by computing annual averages. In order to compress the data in space, yearly averages were saved for every second grid point on four levels (25 m, 250 m, 700 m, 2000 m). Two POP modes account for most of the variance. The leading POP mode capturing 71% of the total variance has a rotation period of 841 years and a damping time of 745 years. The second most energetic mode explaining 25% of the variance has a rotation period of 295 years and a damping time of 282 years.

As the higher-frequency oscillation is locally confined, a regional POP analysis was performed to enhance the signal. The analysis focused on the Southern Ocean where the decadal variability was strongest. We used the annual mean vertical velocity at 50 m, the density at 25 m and 250 m, and the sea ice thickness simultaneously and restricted the POP analysis to a 500-yr period, which is sufficiently long to resolve the decadal variability. The leading POP mode of this regional analysis, explaining 42% of the combined variance, has a rotation period of 20 years and a damping time of 149 years. The existence of three timescales can readily be seen in the three index time series (Fig. 7).

The e-folding time of the decadal POP mode only is much longer than its corresponding rotation period, as expected for self-sustained oscillations. As can be inferred from Fig. 9, the POP coefficient time series of the two longer-timescale modes are highly asymmetric. Apparently, the damped harmonic oscillator assumption is not fulfilled for these two POP modes, which is reflected in the relatively short e-folding times. However, as will be shown below, the fundamental dynamics of the dominant variations are well captured by the two POP modes.

The POP coefficient time series of the lowest frequency mode (Fig. 9a) visualize that this mode is clearly associated with the strongest events seen in the
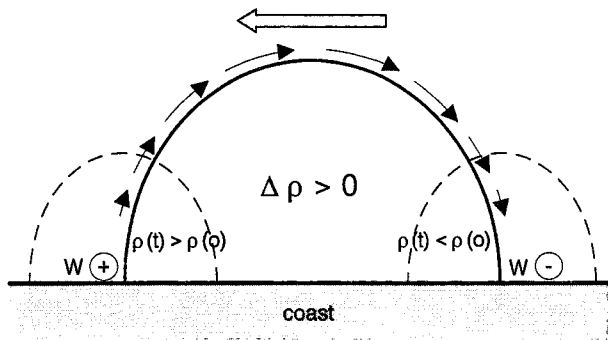
FIG. 12. Schematic of the propagation of the 20-yr mode.

three index time series. The real part POP time series exhibits sawtooth character, while the imaginary part time series is more symmetric. The nature of the two POP coefficient time series suggests that this mode is inherently nonlinear. We return to this point below when we discuss the physics of the different modes. The corresponding autospectra of the POP coefficient time series (Fig. 10a) show peaks near a period of about 1100 years, which is apparently a better timescale estimate than the rotation period given by the POP analysis itself (see Xu and Storch 1990 for a discussion of this issue). The autospectra of the POP time series of the second most energetic mode indicate a period of about 360 years (Fig. 10b) relative to the POP estimate of 295 years. The most regular behavior is found for the 20-yr POP mode (Fig. 9c), with sharply peaked autospectra (Fig. 10c).

The POP coefficient time series of the second most energetic POP mode (Fig. 9b) show not only variability on timescales of about 300 years, but also on the 1100-yr timescale. This suggests that the two modes interact with each other. In order to gain more insight into the nature of this interaction, we computed the complex correlation r_{ij}

$$r_{ij} = \frac{\langle A_i A_j^* \rangle}{\langle A_i A_i^* \rangle^{1/2} \langle A_j A_j^* \rangle^{1/2}} \quad (4.1)$$

and the nonlinear interaction coefficient b_{ij}

$$b_{ij} = \frac{\langle A_i A_i A_j^* \rangle}{[\langle A_i A_i^* \rangle \langle A_i A_i^* \rangle \langle A_j A_j^* \rangle]^{1/2}} \quad (4.2)$$

of the two (complex) POP coefficient time series, as defined by Barnett (1990). In these formulas, A_i and A_j denote the coefficient time series of the 1100-yr and 360-yr POP modes, respectively. The asterisk denotes the complex conjugate of a POP coefficient time series. As described by Barnett (1990), only linear relationships will be disclosed by the complex correlation [Eq. (4.1)] but not nonlinear ones. On the other hand, the simplest measure of nonlinear interactions between the two timescales is given by the nonlinear interaction co-

efficient [Eq. (4.2)]. The absolute value B_{ij} of b_{ij} provides a quantitative measure of the degree to which variations in the two time bands are harmonically coupled to each other. One can view (4.2) also as a measure of the correlation between the energy of the 1100-yr POP mode and the amplitude of the 360-yr POP mode. We computed first the complex correlation r_{ij} between the two POP coefficient time series. The value of r_{ij} attains a value of 0.22 only. Thus, there is no significant linear relationship between the two POP modes (no correlation with zero phase lag). In contrast, the nonlinear interaction coefficient is highly significant, with a value of $B_{ij} = 0.85$. This means that there is significant phase locking between the 1100- and 360-yr POP modes. The phase $\theta_{ij} = \tan^{-1} (\mathrm{Im}b_{ij}/\mathrm{Re}b_{ij})$ amounts to $-106°$, which means that energy fluctuations in the 1100-yr band lag variations in the 360-yr band by about 150 years [for a discussion of the meaning of the phase angle see Barnett (1990)]. This suggests, together with the sawtooth character of the real part of the 1100-yr mode, that the 360-yr mode triggers the 1100-yr mode, when some dynamical quantity associated with the 1100-yr mode has become extreme enough. In the next section, we will further discuss the dynamics of this coupling.

5. Internal variability: A dynamical description

a. The role of convection

The three modes described in the former section have similar characteristics. They consist of a periodic enhancement of AABW formation and ACC transport, which is correlated with a decrease in NADW formation and Atlantic heat transport (Fig. 7). The enhancement of AABW formation is caused by a convective feedback. A positive density anomaly at the surface enhances convection and brings warmer and saltier water upward in the Southern Ocean. The anomalous heat is quickly lost to the atmosphere. So, the positive density anomaly at the surface is enhanced by convection. Thus, convection acts as a positive feedback.

Due to the subsequent increase of vertical mixing the feedback diminishes. Anomalous strong convection causes an erosion of the inverse temperature and salinity gradient. By this process, convection itself destroys the positive feedback. Negative feedbacks may be provided by downwelling and horizontal advection of the anomaly out of the convective action region. After the decrease in convection a stronger density stratification is established due to the production of extra dense bottom or intermediate water in the period before. A period of anomalous weak convection follows. Subsurface heat and salinity transport destabilize the vertical column again. When part of the original anomaly is returned by advection the cycle repeats. The whole chain of feedbacks differs in detail for each oscillation. However, all three are characterized by a periodic in-
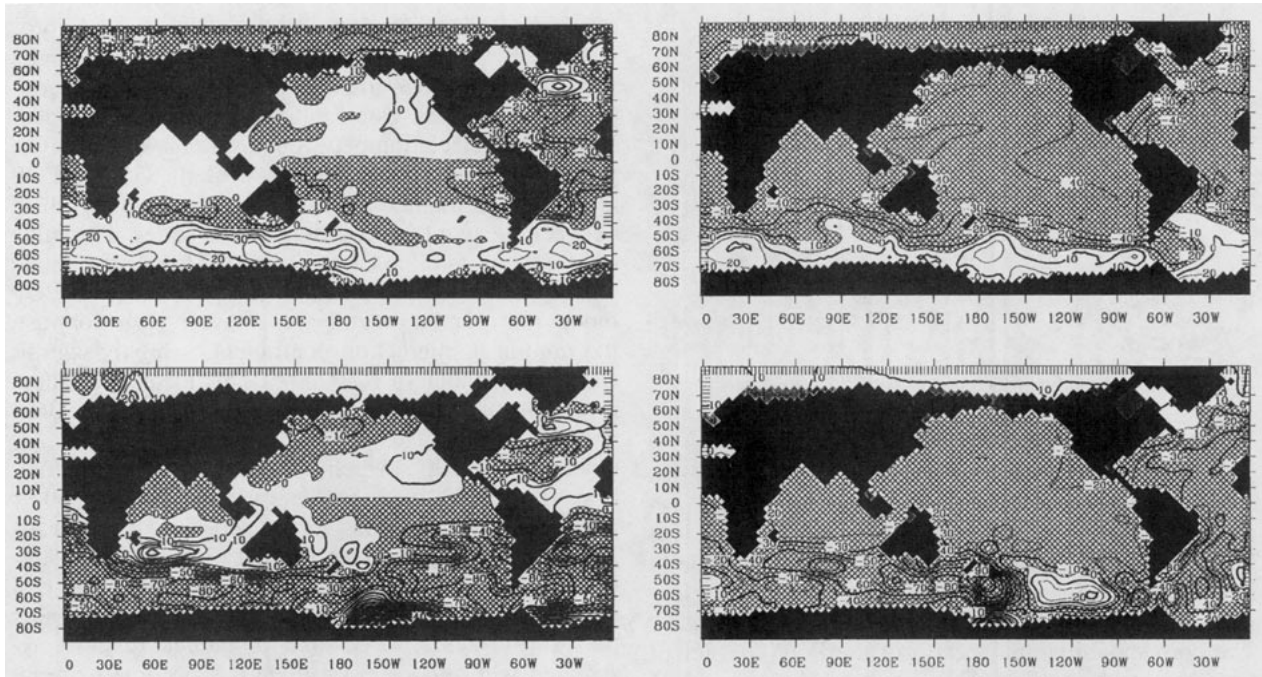
FIG. 13. POP pattern of potential density of 360-yr mode at (a) 25 m (in 10^{-6} kg m^3), (b) 700 m, and (c) 2000 m (in 10^{-9} kg m^3) (above: the real part, below: the imaginary part).

crease of AABW formation provided by a positive convective feedback acting on a surface density (salinity) anomaly.

b. The 20-yr mode

This mode consists of westward traveling density anomalies along the coast of Antarctica (Fig. 11a). In the positive p_1 phase the strongest signal is situated at 110°E. One-quarter of a cycle later, it has a double-cell structure with maxima at 30°E and 80°E. After one-half cycle the anomaly is at 50°W in the Weddell Sea. Here, the signal penetrates deeper by convection. The density and salinity changes, however, are mainly confined to the upper 250 m. The enhancement of convection causes a (short peak) in AABW formation and ACC transport (Fig. 8). The duration of this peak is about 2 years, corresponding to the travel time through the region of convective action. Westward advection of the anomaly provides for the subsequent negative feedback. Thereafter, the anomaly is considerably weakened.

Within the South Indian Basin (Wikes sector) the convective feedback reinforces the anomaly. The anomaly is advected out of the convective region before it is large enough to enhance AABW formation. It is preconditioned in the South Indian Basin for inducing a peak in AABW formation in the Weddell Sea. In the POP patterns, this looks like, as if the signal dies out west of the Weddell Sea and develops again in the south Indian basin (Fig. 11). The 20-yr mode has a

zonal wavenumber two structure, and the period corresponds to the travel time between the south Indian basin and the Weddell Sea.

The positive density anomaly is coupled to a negative sea ice thickness anomaly (Fig. 11b). The sea ice thickness anomaly slightly leads the density anomaly, as was inferred from the raw time series (not shown). This indicates that sea ice might play an active dynamical role in this oscillation. A negative sea ice anomaly induces anomalously strong heat loss to the atmosphere. This enhances convection, which brings saltier water upward. A density anomaly is established that is dominated by salinity through the positive convective feedback. Thus, the sea ice anomaly triggers a heat anomaly, which sets the stage for the development of a salinity-dominated density anomaly through anomalous convection. Thereafter, the density anomaly determines the dynamics and the size of the sea ice thickness anomaly.

Through geostrophy the positive density anomaly induces a cyclonic circulation that is not closed, due to the coast. This causes upwelling on the western side of the anomaly that increases density and downwelling on its eastern side, which decreases density (Fig. 12). As a consequence, the anomaly moves westward. The westward velocity is determined through the efficiency by which upwelling and downwelling change the density around the anomaly. This efficiency is mainly determined by the ratio of the vertical and horizontal scale of the density anomaly. Thus, the dynamics are different from a coastally trapped wave, and the
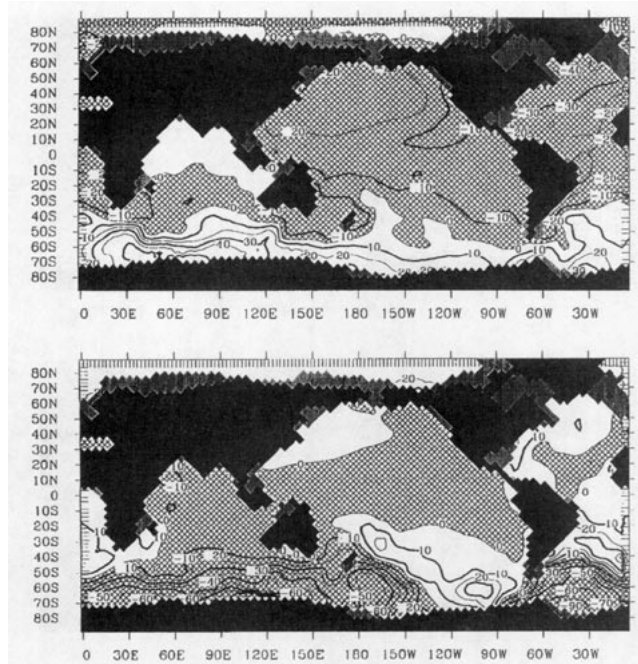
FIG. 13. (Continued)

meridional extent of the anomaly is also much larger $O(1000$ km$)$. Note that the anomaly propagates westward along the coast of Antarctica, south of the eastward flowing ACC.

c. The 360-yr mode

The 360-yr oscillation shows also pronounced variability on the 1100-yr timescale: every third cycle shows an increased amplitude (Fig. 9). Figure 13 shows the spatial pattern of the POP at 25 m, 750 m, and 2000 m. We distinguish five phases (Fig. 14 shows a schematic for this oscillation). The first phase consists of a strengthening positive density anomaly in the upper layers, centered at 155°W near the coast of Antarctica, which is brought about by enhanced convection in the Ross Sea. The convective feedback provides for upwelling of more saline water to the surface and downwelling of fresher and colder water. This reduces the vertical stratification and increases the density through the whole vertical column. As the stratification decreases, the net downwelling associated with AABW formation increases. This increase is balanced by increased advection of fresher surface waters from the north. Also, the convectively upwelled subsurface waters become less saline due to the decreased stratification. At a certain point the horizontal exchange starts to dominate the vertical exchange in the surface salinity budget and the surface anomaly decreases. The anomaly is no longer surface trapped by the convective feedback. It downwells with newly formed AABW and

moves eastward, advected by the ACC. This is the second phase.

Below 1000 m or so, eastward advection is small, and the anomaly spreads slowly northward while it downwells farther to about 2000 m. Eventually, it reaches the upwelling branch of the Southern Ocean THC, south of the subpolar front convergence. Just south of the Agulhas retroflection it reappears in the surface layers (Fig. 13a). In the next, fifth phase, the ACC advects the upwelled anomaly eastward. At the same time the flow converges to the south replacing the downwelling AABW. When it reaches the Ross Sea the cycle repeats itself.

The oscillation can be interpreted as a density anomaly that overturns in the "AABW conveyor belt." When a positive anomaly is present in the surface layers of the Ross Sea, preconditioning is not necessary to start the oscillation. The associated change in AABW formation and vertical stratification is rather modest. This is contrary to the 320-yr mode in the LSG model (Pierce et al. 1995) and the 1100-yr mode in the present model, which induce much larger changes in the Southern Ocean.

d. The 1100-yr mode

We start the discussion of this oscillation with a short summary of its main characteristics. A positive surface density anomaly in the Weddell Sea is amplified by the convective feedback and flows out into the North Atlantic where it joins the global conveyor belt. Transported to the north, it is downwelled by deep convection associated with NADW formation. Thereafter, it is transported back to the south by the deep western boundary current. Due to the strong stratification associated with the increased AABW formation, it does not upwell in the Southern Ocean but joins the NADW outflow into the Indian Ocean, where it upwells between South Africa and Australia. The Agulhas retroflection and ACC advect the anomaly back to the Ross
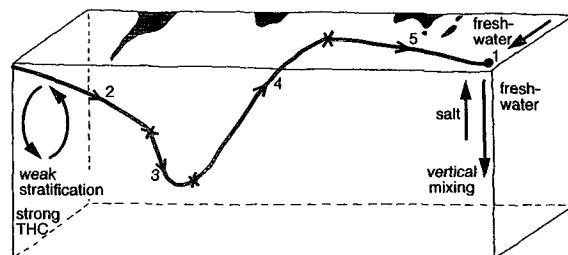
1 amplication by convective feedback
2 downwelling with AABW formation, eastward advection by ACC
3 downwelling and northward spreading with AABW
4 upwelling south of subpolar front convergence
5 southeastward advection by ACC
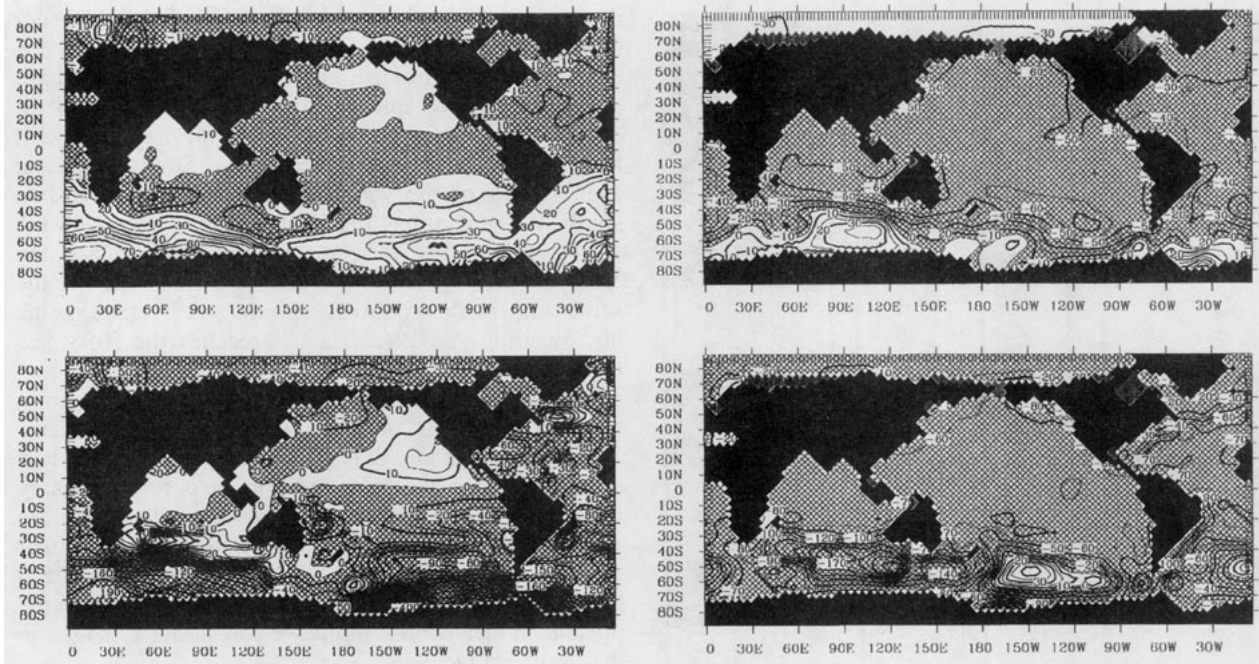
FIG. 14. Schematic for the 360-yr mode.

FIG. 15. As in Fig. 13 but for the 1100-yr mode.

Sea and a lesser part to the Weddell Sea. At this stage, however, the stratification in the Weddell Sea is still too strong and the anomaly is still too small for the cycle to repeat itself. One cycle of the 360-yr oscillation follows. Thereafter, the conditions are met for the 1100-yr oscillation to repeat itself.

The 1100-yr oscillation is illustrated by the POP patterns (Fig. 15) and a schematic (Fig. 16). In addition, we also display salinity anomalies defined relative to the mean of a full 1100-yr cycle. We have chosen the second cycle for this purpose. ACC transport and AABW formation start to increase about 100 years before they reach maximum values. We index time with respect to the maximum in ACC transport: 90 years before, for instance, will be referred to as year -90.

In the first phase, a surface density anomaly in the Weddell Sea intensifies dramatically. The convective feedback in the Weddell Sea is triggered by anomalous convection in the Ross Sea. At the onset of anomalous convection, the Weddell Sea surface anomaly has been advected from the Ross Sea by the ACC, where the convective feedback already has been active for a longer period. This is illustrated by the salinity anomaly field at year -90. The convective feedback starts being active in the Weddell Sea, while anomalous convection is exhausted in the Ross Sea. The salinity anomalies at 2000 m show negative values in the Weddell Sea and eastward of the Ross Sea (Fig. 17a), indicating enhanced convection. The negative anomaly in the Ross Sea has been advected eastward, as anomalous convection has stopped there, and a positive anomaly develops that is the downwelling surface anomaly.

At year 0, the surface anomalies reach maximum values (Fig. 18a). Eastward spreading of the Weddell Sea anomaly by the ACC into the Enderby sector makes this region convectively unstable. In the Ross Sea a negative surface anomaly develops, indicating further decrease in convection. At deeper levels, the eastward extension of the positive anomaly has reached Drake Passage (Fig. 17b). Increased AABW formation in the Weddell Sea is associated with negative salinity anomalies at 2000 m. The associated anomalous density gradient across Drake Passage, however, is opposite due to a strong anomalous temperature gradient, which overcompensates the anomalous salinity gradient. As a result, stronger zonal density and pressure gradients across Drake Passage and stronger meridional density and pressure gradients across the ACC arise. Both accelerate the ACC. The strong anomalous density gradients in the deep ocean are also seen in the POP patterns (Fig. 15).

After amplification by convection, the salinity anomalies flow out into the Atlantic, advected by the global conveyor belt, and to some extent also into the Pacific (Fig. 18a). In the present model Agulhas leakage is absent. As in the LSG model, the conveyor follows the cold water path. Near Drake Passage it mainly consists of AAIW. Most of the signal is transported in the subsurface upper thermocline. In the Tropics, the signal is almost completely absent in the surface layers, which is consistent with a global conveyor belt that flows at deeper levels there. The dynamical picture is summarized by the meridional streamfunction (globally averaged, and for the Atlantic Ocean only) at year 0 (Fig.
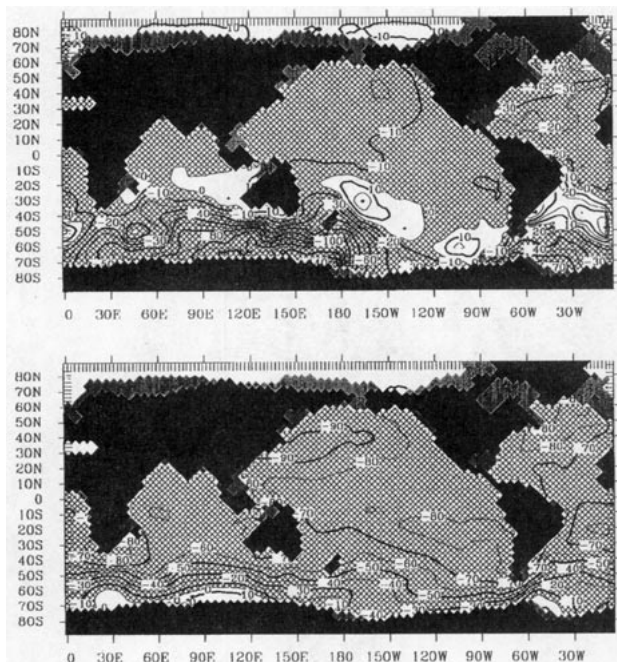
FIG. 15. (*Continued*)

19). The outflow of AABW into the World Ocean has increased by a factor 5 (Fig. 19a vs 3a). This forces the main part of NADW to upwell within the North Atlantic (Fig. 19b). The production of NADW has only slightly diminished (cf. Fig. 3b), but the outflow is reduced by more than 50%. In the Pacific, the enhanced outflow of AABW has increased the equatorial upwelling by a factor of ~2. The northward advected salinity anomaly induces weak North Pacific Bottom Water formation of ~1 Sv at this stage.

In the next phase the density anomaly joins deep convection in the North Atlantic and Pacific. Afterwards it flows out into the deep ocean. In the Atlantic it is quickly transported southward by the deep western boundary current. The Southern Ocean now exhibits negative anomalies everywhere, most intense at the surface, which is associated with a decrease in convection. At year +315, the anomaly has almost completed an overturning cycle in the Atlantic. It has reached the Southern Ocean and is advected eastward into the Indian Ocean (Fig. 17c). At this stage, the density anomaly associated with the corresponding eigenmode found in the LSG model was upwelled to the surface at the polar front, and the cycle repeated itself every 320 years (MMR). In the present model, upwelling is less intense, and the anomaly is advected farther eastward, following a longer path of the conveyor belt. This behavior will be discussed in more detail below.

The positive anomaly, advected within NADW into the Indian Ocean, upwells between Australia and South Africa. Between years +585 and +720, the surface salinity anomalies in the Ross and Weddell Sea change

sign (Figs. 18b and 18c). This reflects the 360-yr cycle. At this stage, advection toward the Ross Sea of the upwelled anomalies of the 360-yr and 1100-yr mode coincide (Fig. 18b). The upwelled density anomaly of the 1100-yr mode is advected by the Agulhas retroflection and ACC. Part of the Ross Sea anomaly is advected by the ACC farther eastward to the Weddell Sea. However, at year +720 (−360), the stratification in the Weddell Sea is still too strong and inflow of positive salinity is still too small for the 1100-yr cycle to repeat itself. Another 360-yr cycle is to follow.

The Ross Sea anomaly displays a minimum again after 135 years. The convective feedback in the Weddell Sea, however, is strong enough for the anomaly to remain positive. When the 360-yr cycle starts to increase the surface salinity in the Ross Sea, the salinity (density) field in the Weddell Sea is preconditioned for a dramatic enhancement of deep convection. The anomaly is now positive compared to negative 360 years before (Fig. 18b). Also vertical mixing has further eroded the stratification. Now, eastward advection toward the Weddell Sea of the Ross Sea positive salinity anomaly associated with the 360-yr cycle triggers the 1100-yr cycle again.

e. Physical mechanism

As discussed above, the 1100-yr mode in the present model resembles in some parts the 320-yr mode found in the LSG model. Both consist of density (salinity) anomalies periodically inducing strong peaks in AABW formation and ACC transport. Thereafter, in both cases the anomalies are advected northward by the global conveyor belt into the Atlantic and return southward with the advective path of NADW. In both cases, this takes about 300 years. However, in the LSG model, the anomaly upwells at the Southern Hemisphere Polar Front inducing another event. In the present model, the
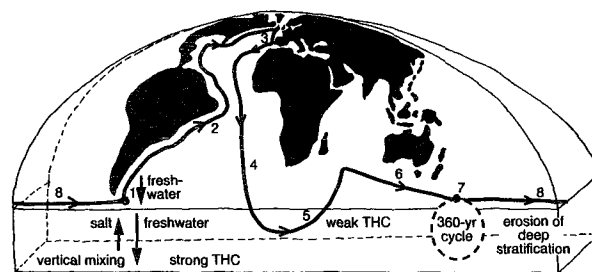
1 amplification by convective feedback in Weddell Sea
2 northward advection with upper branch of Conveyor Belt
3 downwelling with NADW formation
4 southward advection with Deep Western Boundary Current
5 eastward spreading into Indian Ocean, upwelling
6 southeastward advection by ACC
7 amplification in Ross-Sea, 360-yr cycle
8 eastward advection by ACC, erosion of deep stratification by diffusion
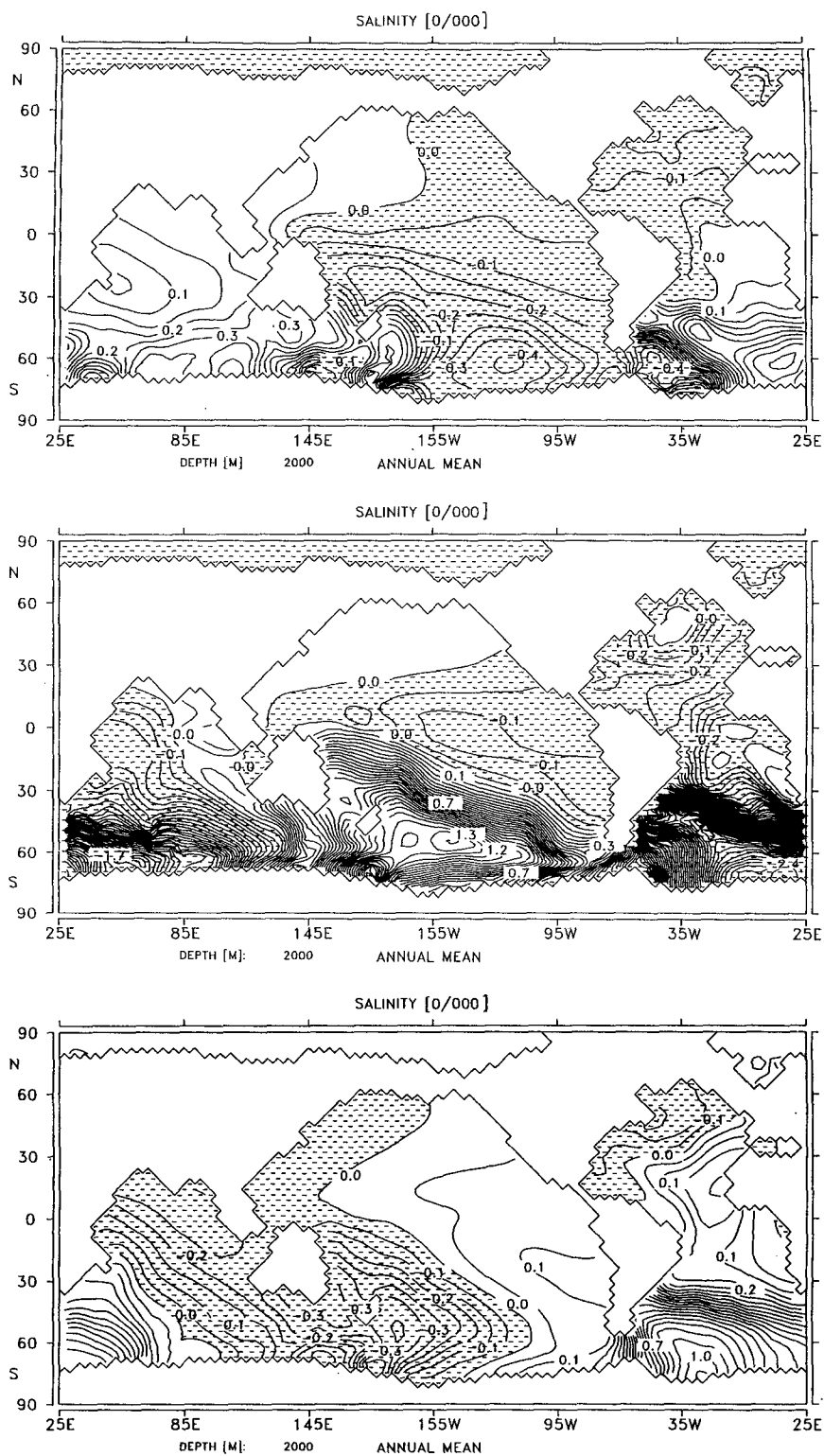
FIG. 16. Schematic for the 1100-yr mode.

FIG. 17. Salinity anomaly for the 1100-yr mode at 2000-m depth in 0.1 psu at (a) year −90,
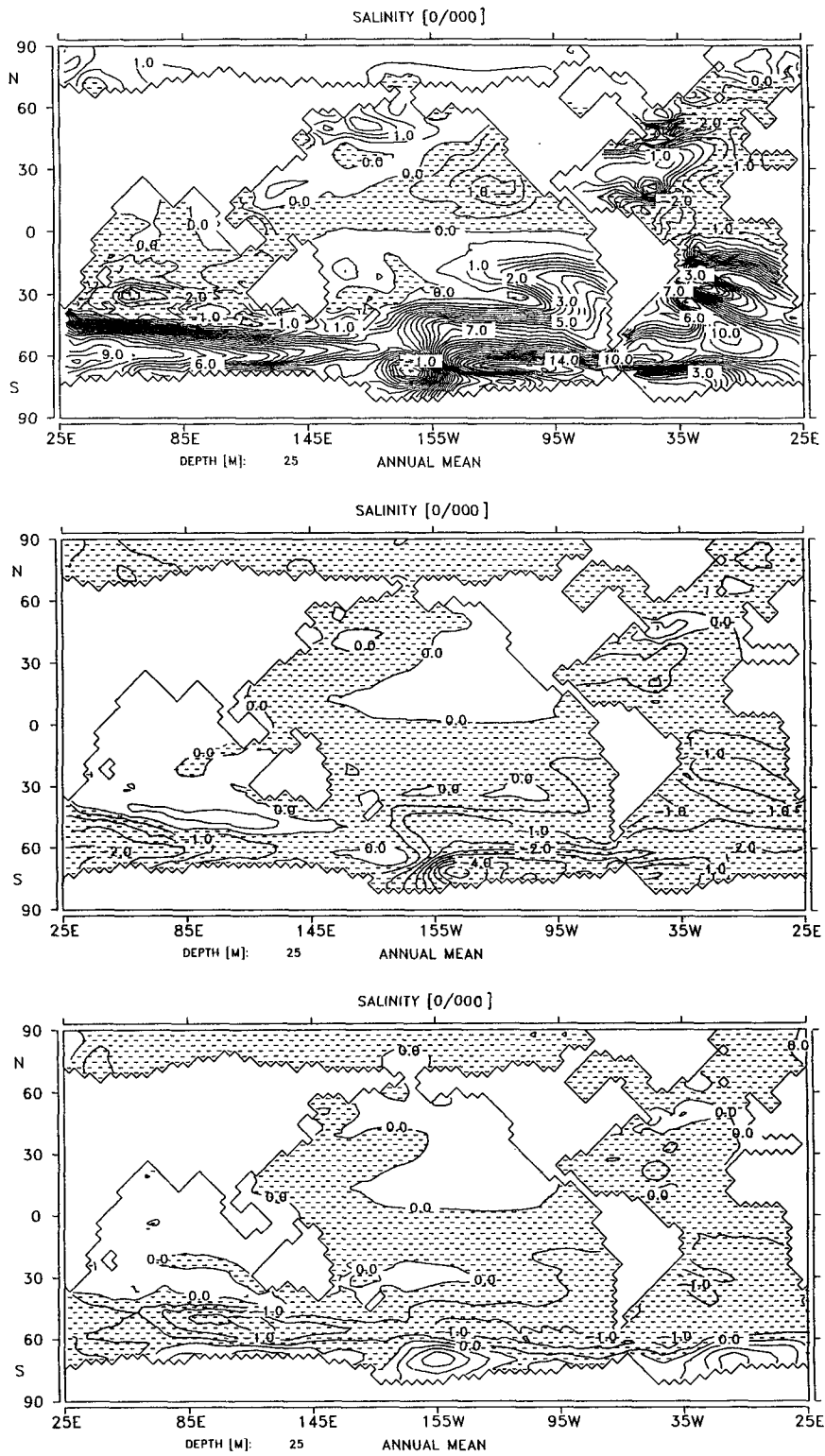(b) year 0, and (c) year +315 (years relative to peak in AABW formation).

FIG. 18. Salinity anomaly at 25-m depth in 0.1 psu at (a) year 0, (b) year +585, and (c) year +720.
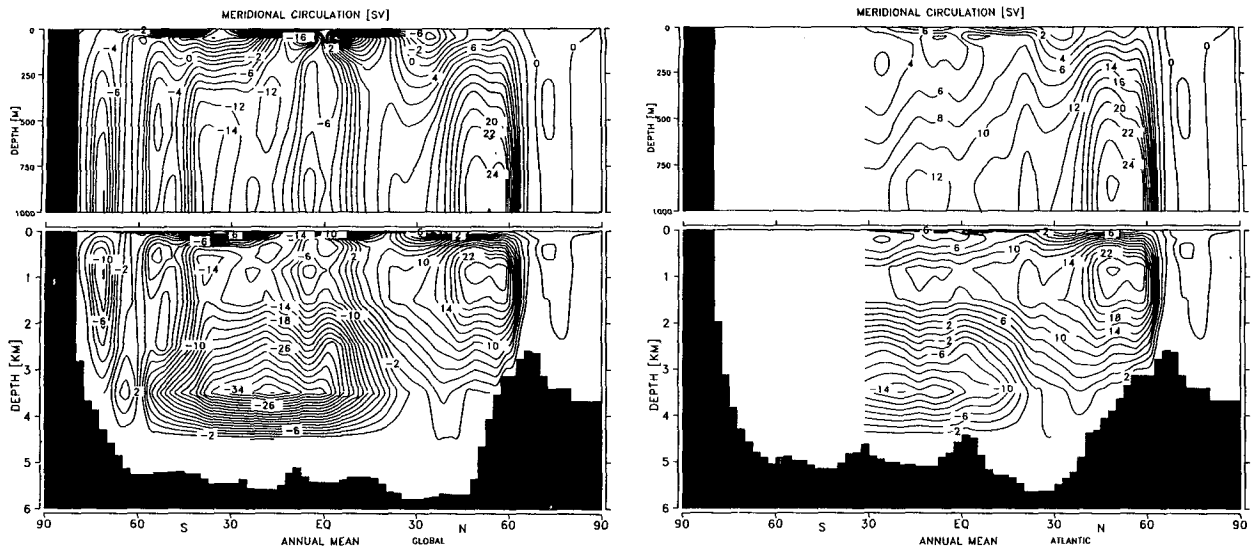
FIG. 19. Global meridional overturning circulation, and meridional overturning circulation in the Atlantic
at the 1100-yr peak in AABW formation.

upwelling is weaker, especially after the event of increased AABW formation, which strengthens the density stratification in the Southern Ocean. The anomaly is advected with the NADW and spreads into the Indian and Pacific Oceans. The timescale of the most prominent eigenmode is influenced by the strength of the THC in the Southern Ocean, which is strongly coupled to the effective diffusion (see section 3). The effective diffusion is much smaller in the present model relative to the LSG, and the timescale of the oscillation is much longer.

The difference in effective diffusion, however, cannot explain alone the differences between the dominant eigenmodes in the two models. Pierce et al. (1995) have shown that in the LSG the eigenmode is forced by surface freshening and subsurface heating. In both the LSG and present model the stratification in the Southern Ocean is such that the models can easily oscillate between a strong and a weak THC. In the LSG model the steady state shows a strong THC. This state is unstable for negative salinity anomalies, which are amplified by the convective feedback. The LSG model periodically shows the amplification of a negative SSS anomaly, which shuts off convection in the Southern Ocean. The subsequent reduction in heat loss to the atmosphere leads to a subsurface increase of heat and salinity by advected NADW. The restratification is associated with a decrease of the density at intermediate depths. Eventually (within 100 years), the water column becomes unstable again, and the model jumps to a state that modestly overshoots the steady-state strong THC. Quickly, however, the stratification and THC return to the steady-state values. Now the model is preconditioned again for another THC collapse. The time-

scale of 320 years cannot be explained by the subsurface heating alone. It seems to be related to the overturning time of salinity anomalies within the Atlantic.

In the present model the steady state shows a weak THC, which is unstable for positive salinity anomalies that are amplified by the convective feedback. Associated with this mechanism is a periodic jump to a strong THC. The strong THC, however, can only be maintained as long as the convective feedback provides for anomalous transport of salt from intermediate depth to the surface. In the present model subsurface heat and salinity transport by advected NADW is much less compared to the LSG model due to a reduced effective diffusion. As a result, the strong THC cannot be maintained and the SSS anomaly and THC decrease quickly after the model has jumped to the strong THC. During the strong THC anomalous cooling associated with anomalous convection produces extra dense bottom waters. When the THC weakens again, the model jumps to a state of anomalous weak THC and an anomalously strong stratified deep ocean. The model slowly recovers to the steady-state THC by heating of the deep ocean. This heating is provided by vertical diffusion of the heat and salinity of advected NADW at intermediate depth.

The recovery after each strong event is reflected by the sawtooth character of the real POP coefficient time series of the 1100-yr mode (Fig. 9). Figure 20 shows that the recovery is associated with the water mass characteristics of the deep ocean. After each strong event an extra amount of AABW is formed, which makes the deep ocean fresher, colder, and denser. For the next thousand years, the deep ocean recovers from
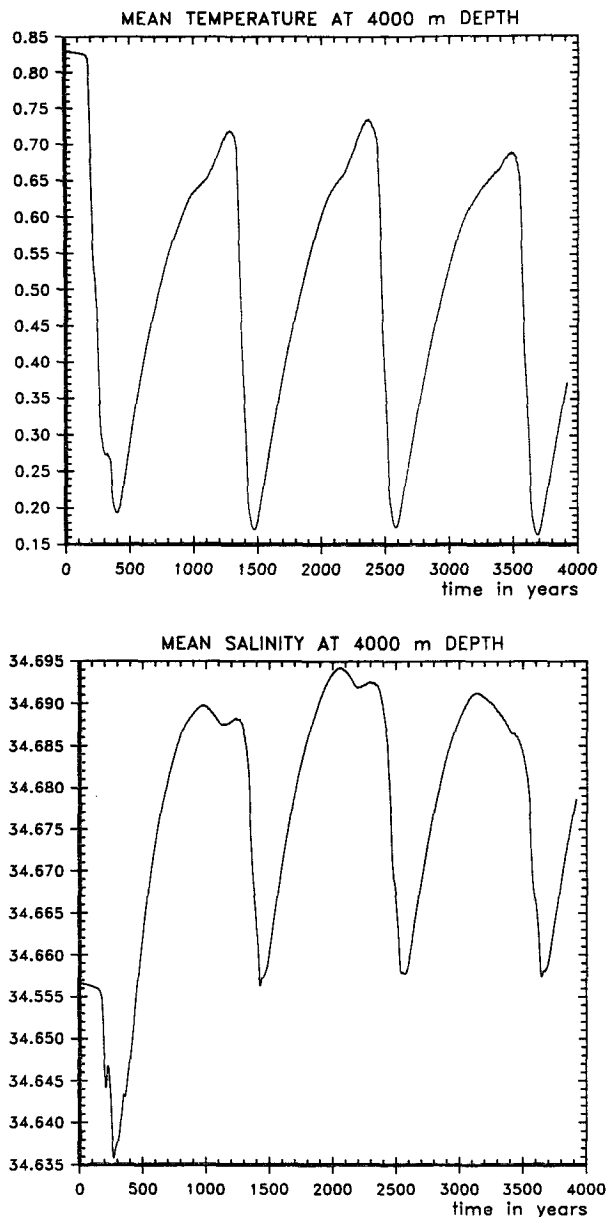
FIG. 20. Time series for globally averaged potential temperature and salinity at 4000-m depth.

progresses from one event to the next. In the MMR mode the increase at intermediate depth as shown by Pierce et al. is most prominent. From Fig. 21 it also can be seen that 360 years prior to the mean event a slight decrease of stratification takes place, associated with the 360-yr cycle. However, at this stage the deep ocean is still too strongly stratified for a large event to take place.

The different modes in MMR and the present study are influenced by the different effective diffusion in the two models. Associated with this is the different amount of advected NADW in the Southern Ocean and the different path of the main core of NADW through the World Ocean. As a result, the turnover timescale for salinity anomalies is much larger in the present model. The effect of these differences on the most prominent eigenmode is summarized in Fig. 22.

The effective vertical diffusion in the LSG model might be too strong, and vertical sections along GEO-SECS tracks of potential temperature and salinity illustrate that the reduced vertical diffusivity in the present model is more favorable. However, AABW formation and ACC transport are clearly too weak, and we can certainly not conclude that the vertical stratification in the Southern Ocean is modeled better. In this region, mixing by eddies might be important, and a low-resolution model with an upstream scheme might come closer to the truth in this region than a low-resolution model with a second-order scheme and weaker effective vertical diffusion. At the present level of knowledge, we can conclude only that the timescale of the dominant eigenmode of an ocean model is set by the very poorly known vertical diffusion and that we cannot say which one, if any, is the right one.

6. Summary and conclusions

In this paper, we describe a primitive equation World Ocean model. It is globally applicable and includes a free surface and a dynamic/thermodynamic sea ice model with viscous–plastic deformation physics. We investigated the steady state obtained by running the model with restoring boundary conditions and the behavior under mixed boundary conditions. The model was forced by boundary conditions close to the forcing of the reference run of the LSG model (MMH) to make comparison possible. For the present model the spun-up model state is not considered as the best possible. Tuning of parameters and boundary conditions is still going on in order to achieve an optimal model hydrography in parallel with a realistically strong ACC.

The model shows deep-water formation in the northern North Atlantic and the Southern Ocean. In the present model version, the characteristics of AABW are too cold and too fresh. This might be so because the Levitus salinity climatology is biased toward too low salinity values near Antarctica, as winter measurements of salinity near Antarctica are rather scarce. The effective

this event by gradually increasing its salinity and temperature, thereby decreasing its density. It is seen that the sawtooth character of the real part of the POP is best reproduced by the time series of globally averaged temperature at 4000 m. The salinity partly compensates this effect.

The different scenarios for the eigenmodes in the LSG and present model are illustrated by comparing the time evolution of the vertical temperature and salinity in the Weddell Sea (Fig. 21 and Fig. 8 of Pierce et al.). Gradients in the deep ocean decrease as time
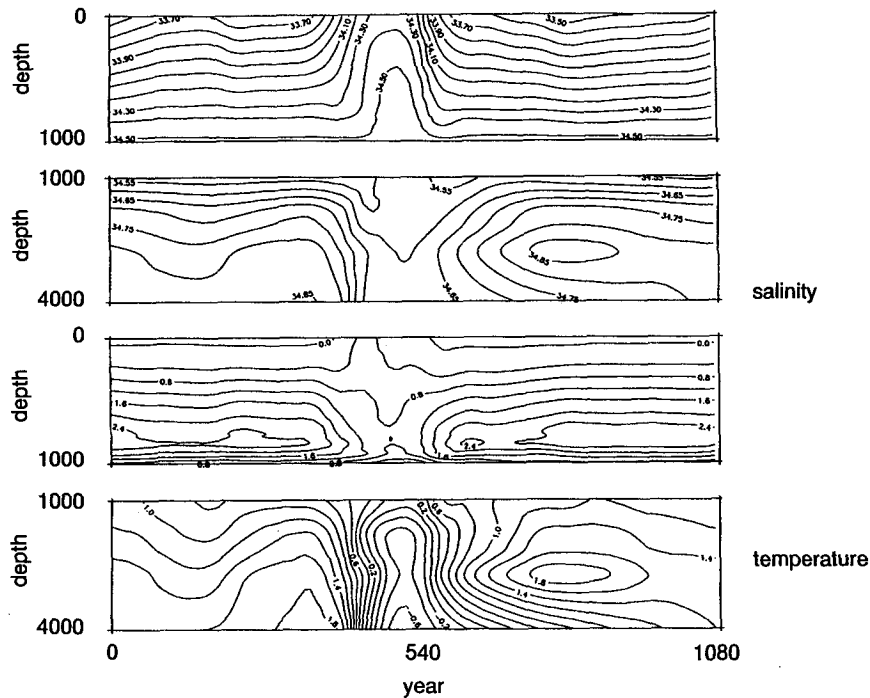
FIG. 21. Time versus depth contours of model fields averaged over the Weddell Sea: (a) temperature, (b) salinity. Time goes from 0 to 1080 years with a peak in AABW formation at year 540. As the oscillation is almost periodic, year 0 and 1080 (almost) coincide.

freshwater fluxes that arise from the restoring condition on sea surface salinity have been diagnosed in steady state, and the model was integrated further prescribing these freshwater fluxes (mixed boundary conditions). The ocean circulation undergoes self-sustained oscillations over a wide range of timescales, ranging from decadal to millennium.

Three POP modes were discussed. The leading mode is associated with a positive salinity anomaly that is advected by the global conveyor belt. It has a timescale of 1100 years and is associated with large excursions in the Drake Passage transport, reductions in NADW outflow, and Atlantic heat transport. The second POP mode having a timescale of 360 years consists of a salinity anomaly that is advected by the Southern Ocean THC. The third POP mode has a period of 20 years and consists of a coupled density/sea ice thickness anomaly propagating westward along the coast of Antarctica. All three oscillations are determined by surface density anomalies in the Southern Ocean that consist mainly of salinity anomalies. Both convection and air–sea interaction periodically amplify the surface density anomalies through the coupling between increased convection and an intensification of the ACC, which reduces the exposure time to the region of maximum freshwater gain in the Southern Ocean. Eventually, the anomalies equilibrate and start diminishing through the changed circulation, which provides for the negative feedback.

The timescale of the 20-yr mode is determined by horizontal advection. Geostrophy induces a cyclonic circulation in response to a positive density anomaly. Near the Antarctic coast, upwelling is found on the western side of the anomaly, downwelling on its eastern side. This increases the density on the western side and the anomaly moves westward. No equivalent of the Weisse et al. (1994) decadal oscillation was found. The 360-yr and 1100-yr modes are coupled. The shorter one overturns in the AABW conveyor belt. The periodic weakening of the stratification in the Southern Ocean helps to excite the strong events associated with the 1100-yr oscillation. The 1100-yr oscillation follows the global conveyor belt and resembles the 320-yr mode simulated by the LSG model. After overturning in the Atlantic Ocean, the anomaly is advected with the NADW and spreads into the Indian and Pacific Oceans. A period of erosion of the density stratification in the Southern Ocean follows the upwelling before the cycle repeats itself. Then, the next 360-yr cycle triggers the 1100-yr cycle. The timescale of the 1100-yr mode seems to be determined by the effective vertical diffusion in the model.

The largest part of the anomaly associated with the 1100-yr mode is mixed away along its advective path. At the end of an overturning cycle typically a few percent of the signal has survived. Due to the existence of the convective feedback in a region that is marginally stable, one fragment of the scattered anomaly is am-
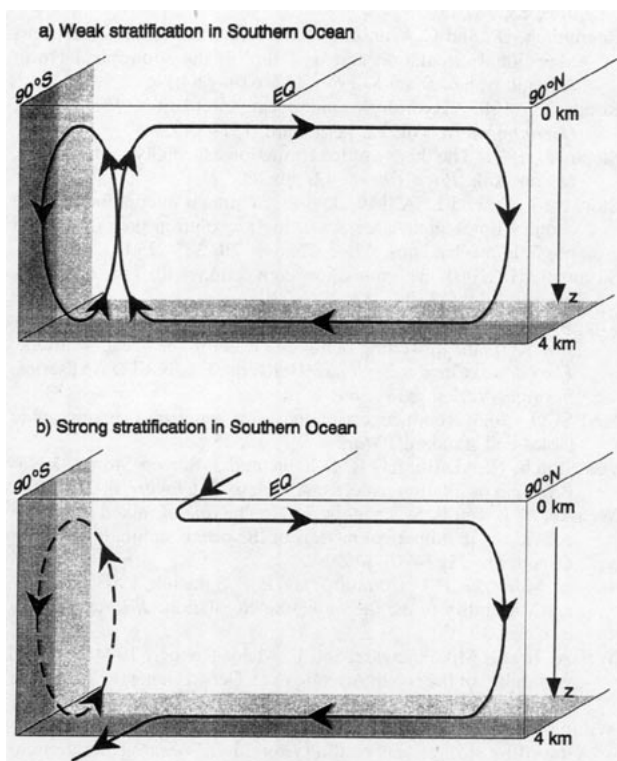
Atlantic Meridional Circulation

FIG. 22. Schematic for the pathway of salinity anomalies in the Atlantic for different THC in the Southern Ocean.

plified to its original amplitude. Whether the inclusion of atmospheric noise would change the characteristics of the eigenmode is uncertain. We hypothesize that the propagation of the anomaly will not be altered significantly. Most of the pathway is beneath the surface, and as stated before, only a small fragment of the anomaly has to propagate along the whole path to trigger a new cycle. This is consistent with the findings of Pierce et al. (1995), who are able to recover the same eigenmode in the LSG model with and without noise forcing. To what extent the amount of AABW formation and the strength of the ACC influence the eigenmode is also unclear. Comparing the LSG and present model, it seems possible that the strength and nature of the Southern Ocean THC determine the nature of this type of long-timescale variability. The sensitivity of this mode to the steady state and inclusion of noise forcing will be investigated with the next cycle of the model, which simulates a more realistic ACC transport and AABW formation rate.

Century-timescale variability has also been found in other models, for example, Winton and Sarachik (1993). Evidence for variability in the earth's climatic system on these timescales was described by, for example, Stocker and Mysak (1992). However, at the present level of knowledge, it seems impossible to conclude on the robustness of the century-scale eigenmodes found in numerical models. They appear to be highly sensitive to details of the freshwater flux forcing (Weaver et al. 1993), details of the heat flux forcing (MMH), the convective adjustment (Lenderink and Haarsma 1994), and the parameterization of vertical and horizontal diffusion. The strong sensitivity of the ocean circulation to these processes may be real but seems at least partly due to the absence of a realistic atmospheric feedback. The inclusion of more realistic feedback models yield ocean model simulations with strongly reduced sensitivity (Rahmstorf and Willebrand 1995). At present, we do not know whether the eigenmodes discussed here are insensitive to a more sophisticated coupling strategy.

However, that these century-scale eigenmodes are found in rather different numerical models and under rather different atmospheric forcings seems to be a strong indication that they have at least some relevance with respect to the real world.

REFERENCES

Arakawa, A., and V. R. Lamb, 1977: Computational design of the basic dynamical processes of the UCLA General Circulation Model. *Methods Comput. Phys.,* **17,** 173–265.

Barnett, T. P., 1990: The interaction of multiple time scales in the tropical climate system. *J. Climate,* **3,** 269–285.

Broecker, W. S., M. Andree, W. Wolfli, H. Oeschger, G. Bonani, J. Kennet, and D. Peteet, 1988: The chronology of the last deglaciation: Implications to the cause of the younger Dryas event. *Paleoceanogr.,* **3,** 1–19.

Bryan, F., 1986: High-latitude salinity effects and interhemispheric thermohaline circulations. *Nature,* **323,** 301–304.

Cox, M., 1984: A primitive equation, 3-dimensional of the ocean. GFDL Ocean Group Tech. Rep. No. 1, 141 pp.

Delworth, T., S. Manabe, and R. J. Stouffer, 1993: Interdecadal variations of the thermohaline circulation in a coupled ocean–atmosphere model. *J. Climate,* **6,** 1993–2011.

England, M. H., 1993: Representing the global-scale water masses in ocean general circulation models. *J. Phys. Oceanogr.,* **23,** 1523–1552.

Frankignoul, C., and K. Hasselmann, 1977: Stochastic climate models. Part II: Application to sea-surface temperature anomalies and thermocline variability. *Tellus,* **29,** 419–426.

Gerdes, R., C. Köberle, and J. Willebrand, 1991: The influence of numerical advection schemes on the results of ocean general circulation models. *Climate Dyn.,* **5,** 211–226.

Hasselmann, K., 1976: Stochastic climate models. Part I: Theory. *Tellus,* **28,** 473–485.

——, 1988: PIP's and POP's: The reduction of complex dynamical systems using principal interaction and oscillation patterns. *J. Geophys. Res.,* **93,** 11 015–11 021.

Hellerman, S., and M. Rosenstein, 1983: Normal monthly wind stress over the World Ocean with error estimates. *J. Phys. Oceanogr.,* **13,** 1093–1104.

Hibler, W. D., 1979: A dynamic thermodynamic sea ice model. *J. Phys. Oceanogr.,* **9,** 815–846.

Killworth, P. D., D. Stainforth, D. Webb, and S. M. Patterson, 1991: The development of a free-surface Bryan–Cox–Semtner ocean model. *J. Phys. Oceanogr.,* **21,** 1333–1348.

Latif, M., 1987: Tropical ocean circulation experiments. *J. Phys. Oceanogr.,* **17,** 246–263.

——, T. Stockdale, J. Wolff, G. Burgers, E. Maier-Reimer, M. M. Junge, K. Arpe, and L. Bengtsson, 1994: Climatology and variability in the ECHO coupled GCM. *Tellus,* **46,** 351–366.

Lenderink, G., and R. J. Haarsma, 1994: Variability and multiple equilibria of the thermohaline circulation associated with deep-water formation. *J. Phys. Oceanogr.,* **24,** 1480–1493.

Levitus, S., 1982: *Climatological Atlas of the World Ocean.* NOAA Prof. Paper No. 13, U.S. Govt. Printing Office, 173 pp.

Maier-Reimer, E., U. Mikolajewicz, and K. Hasselmann, 1993: Mean circulation of the Hamburg LSG OGCM and its sensitivity to the thermohaline surface forcing. *J. Phys. Oceanogr.,* **23,** 731–757.

Manabe, S., and R. J. Stouffer, 1988: Two stable equilibria of a coupled ocean–atmosphere model. *J. Climate,* **1,** 841–866.

Marotzke, J., 1990: Instabilities and multiple equilibria of the thermohaline circulation. Ph.D. thesis, Institut Meereskunde Kiel, 126 pp.

——, P. Welander, and J. Willebrand, 1988: Instability and multiple steady states in a meridional-plane model of the thermohaline circulation. *Tellus,* **40A,** 162–172.

Mikolajewicz, U., and E. Maier-Reimer, 1990: Internal secular variability in an OGCM. *Climate Dyn.,* **4,** 145–156.

——, and ——, 1994: Mixed boundary conditions in OGCM's and their influence on the stability of the model's conveyor belt. *J. Geophys. Res.,* **99,** 22 633–22 644.

Moore, A. M., and C. J. C. Reason, 1993: The response of a global ocean general circulation model to climatological surface boundary conditions for temperature and salinity. *J. Phys. Oceanogr.,* **23,** 300–328.

Pierce, D. W., T. P. Barnett, and U. Mikolajewicz, 1995: On the competing roles of heat and freshwater flux in forcing thermohaline oscillations. *J. Phys. Oceanogr.,* **25,** 2046–2064.

Rahmstorf, S., and J. Willebrand, 1995: The role of temperature feedback in stabilizing the thermohaline circulation. *J. Phys. Oceanogr.,* **25,** 787–805.

Roemmich, D., and C. Wunsch, 1985: Two trans-Atlantic sections: Meridional circulation and heat flux in the subtropical North Atlantic ocean. *Deep-Sea Res.,* **32,** 619–664.

Rooth, C., 1982: Hydrology and ocean circulation. *Progress in Oceanography,* Vol. 11, Pergamon, 131–149.

Stefan, J., 1891: The theory of ice formation especially in the Arctic. *Ocean. Ann. Phys. Chem.,* **42,** pp. 269.

Stocker, T. F., and L. A. Mysak, 1992: Climate fluctuations on the century timescale: A review of high-resolution proxy data and possible mechanisms. *Clim. Change,* **20,** 227–250.

Stommel, H., 1961: Thermohaline convection with two stable regimes of flow. *Tellus,* **13,** 224–230.

Toggweiler, J. R., and B. Samuels, 1993: New radiocarbon constraints on the upwelling of abyssal water to the ocean's surface. *The Global Carbon Cycle,* M. Heimann, Ed., NATO ASI series, Springer-Verlag, 333–366.

UNESCO, 1983: Tenth report of the joint panel on oceanographic tables and standards. *Marine Sci.,* **36,** 25 pp.

von Storch, H., G. Bürger, R. Schnur, and J.-S. von Storch, 1995: Principal oscillation patterns: A review. *J. Climate,* **8,** 377–400.

Weaver, A. J., and E. S. Sarachik, 1991: The role of mixed boundary conditions in numerical models of the ocean's climate. *J. Phys. Oceanogr.,* **21,** 1470–1493.

——, J. Marotzke, P. F. Cummins, and E. S. Sarachik, 1993: Stability and variability of the thermohaline circulation. *J. Phys. Oceanogr.,* **23,** 39–60.

Weisse, R., U. Mikolajewicz, and E. Maier-Reimer, 1994: Decadal variability of the North Atlantic in an Ocean General Circulation Model. *J. Geophys. Res.,* **99,** 12 411–12 421.

Winton, M., and E. S. Sarachik, 1993: Thermohaline oscillations induced by strong steady salinity forcing of ocean general circulation models. *J. Phys. Oceanogr.,* **23,** 1389–1410.

Woodruff, S. D., R. J. Slutz, R. L. Jenne, and P. M. Steurer, 1987: A comprehensive ocean–atmosphere dataset. *Bull. Amer. Meteor. Soc.,* **68,** 1239–1250.

Xu, J.-S., and H. von Storch, 1990: Principal oscillation patterns—Prediction of the state of ENSO. *J. Climate,* **3,** 1316–1329.